Crystalline and amorphous cluster-assembled nano-materials, synthesized with a novel cluster deposition system

Kristalline und amorphe clusterbasierte Nanomaterialien, die mit einer neuartigen Clusterdepositionsanlage synthetisiert wurden

Zur Erlangung des Grades eines Doktors der Naturwissenschaften (Dr. rer. nat.) genehmigte Dissertation von Dipl.-Phys. Arne Stephen Fischer aus Heidelberg
Juli 2015 — Darmstadt — D 17

TECHNISCHE UNIVERSITÄT DARMSTADT

Fachbereich
Material- und Geowissenschaften
Technische Universität Darmstadt

Institut für Nanotechnologie (INT)
Karlsruher Institut für Technologie (KIT)

Crystalline and amorphous cluster-assembled nanomaterials, synthesized with a novel cluster deposition system

Kristalline und amorphe clusterbasierte Nanomaterialien, die mit einer neuartigen Clusterdepositionsanlage synthetisiert wurden

Vom Fachbereich Material- und Geowissenschaften der Technischen Universiät Darmstadt

Zur Erlangung des Grades eines Doktors der Naturwissenschaften (Dr. rer. nat.)

Genehmigte Dissertation von Dipl.-Phys. Arne Stephen Fischer aus Heidelberg

1. Gutachten: Prof. Dr.-Ing. Horst Hahn
2. Gutachten: Prof. Dr. Manfred Kappes

Tag der Einreichung: 30.03.2015
Tag der Prüfung: 05.05.2015

Darmstadt 2015 — D 17

Erklärung zur Dissertation

Hiermit versichere ich, die vorliegende Dissertation ohne Hilfe Dritter nur mit den angegebenen Quellen und Hilfsmitteln angefertigt zu haben. Alle Stellen, die aus Quellen entnommen wurden, sind als solche kenntlich gemacht. Diese Arbeit hat in gleicher oder ähnlicher Form noch keiner Prüfungsbehörde vorgelegen.

Darmstadt, den 27.03.2015

(Arne Stephen Fischer)

Abstract / Zusammenfassung

Abstract

Clusters are generally defined as aggregates of three up to several million atoms or molecules. In recent years, it has been shown, that especially small clusters in the size-range of a few nanometers can exhibit unique, size-dependent properties (e.g. magnetic, electronic), differing them from their bulk material counterparts. Therefore, synthesizing materials based on size-selected clusters may pave the way to new types of materials with tailorable properties.

In order to be able to synthesize any kind of cluster-composed material with a high degree of control over the various material characteristics, a cluster ion beam deposition system was designed, ion-optically simulated, and constructed. Thereby, the focus was to develop a versatile system, that offers as much control as possible over the various deposition parameters.

Experiments on two cluster/matrix nanocomposites, namely iron/silver and iron/chromium, as well as a purely cluster-composed material based on amorphous iron-scandium alloy clusters, were conducted with the newly developed deposition system.

The experiments on iron/silver revealed, that the cluster ion beam deposition system allows to synthesize cluster-composed materials with, amongst other features, an outstanding degree of control in terms of deposited amounts of clusters, and homogeneity of the synthesized samples.

The focus of the experiments on iron/chromium was to thoroughly study the magnetic characteristics of the ferromagnetic (iron)/antiferromatic (chromium) samples. The obtained results yielded insights into the relation between the various magnetic characteristics, for example the exchange bias effect, and the sample parameters, i.e. the size of the embedded clusters and the cluster volume fractions in the samples.

Finally, experiments are presented, where a material purely composed of amorphous Fe-Sc alloy clusters was characterized. The obtained results indicate, that by systematic variation of the deposition parameters, a new amorphous structure with altered properties compared to conventional amorphous material, typically prepared by rapid quenching, was synthesized.

Zusammenfassung

Cluster werden typischerweise als Ansammlung von drei bis zu mehreren Millionen Atomen oder Molekülen definiert. In den letzten Jahren wurde gezeigt, dass inbesondere kleine Cluster im Größenbereich von einigen Nanometern einzigartige größenabhängige Eigenschaften (z.B. magnetische oder elektrische) haben können, die sie von ihren Festkörper-Gegenstücken unterscheiden. Daher könnte die Herstellung von Materialien auf Basis von größenselektierten Clustern den Weg zu neuen Materialklassen mit einstellbaren Eigenschaften ebnen.

Mit dem Ziel, einen weiten Bereich von clusterbasierten Materialien mit einem hohen Maß an Kontrolle über die unterschiedlichen Materialeigenschaften herstellen zu können, wurde eine Cluster-Ionenstrahl-Beschichtungsanlage entworfen, ionenoptisch simuliert und aufgebaut. Das Hauptaugenmerk lag darauf, eine möglichst flexible Anlage zu entwickeln, die eine größtmögliche Kontrolle über die verschiedenen Abscheideparameter bietet.

Mit Hilfe der neuen Beschichtungsanlage wurden Experimente mit zwei verschiedenen Cluster/Matrix Materialsystemen (Eisen/Silber und Eisen/Chrom), sowie einem rein clusterbasierten Material, bestehend aus amorphen Eisen-Scandium Legierungsclustern, durchgeführt.

Unter anderem konnte anhand der Experimente mit Eisen/Silber gezeigt werden, dass es die Cluster-Ionenstrahl-Beschichtungsanlage ermöglicht, clusterbasierte Materialien sehr homogen sowie mit einer herausragenden Kontrolle über die abgeschiedenen Clustermengen herzustellen.

Im Fokus der Experimente mit Eisen/Chrom stand eine sorgfältige Studie der magnetischen Eigenschaften des Materialsystems, das eine Mischung aus ferromagnetischen Clustern (Eisen) und einer antiferromagnetischen Matrix (Chrom) darstellt. Die Ergebnisse ergaben Einblicke in die Zusammenhänge zwischen den verschiedenen magnetischen Eigenschaften des Systems, beispielsweise dem Exchange Bias Effekt, und den grundlegenden Kenngrößen der Proben, wie die Größe der eingebetteten Cluster und den Cluster-Volumenanteilen.

Zuletzt wurde ein Material hergestellt und untersucht, das ausschließlich aus amorphen Eisen-Scandium Legierungsclustern besteht. Die erzielten Ergebnisse deuten darauf hin, dass durch gezielte Veränderung der Abscheideparameter der Cluster eine neuartige amorphe Struktur hergestellt werden konnte. Diese weist gegenüber amorphen Material, das üblicherweise durch schnelles Abschrecken hergestellt wird, deutlich veränderte Materialeigenschaften auf.

Acknowledgments

First of all I would like to thank Prof. Horst Hahn who gave me the opportunity for an interesting and inspiring work in his group at the Institute of Nanotechnology. I am very grateful for his trust and support in realizing my ideas and numerous fruitful discussions over the past years.

I want to thank Prof. Manfred Kappes who agreed to be the co-referee for this dissertation.

Robert Kruk supported me in many aspects and he always had a sympathetic ear when (experimental) problems of any kind arose. I am very grateful for that.

A special thanks goes to my office mate Ralf Witte for innumerable discussions, lots of help with the Mössbauer spectroscopy, for the good atmosphere we always had in the office, and his friendship.

Virgil Provenzano and Richard Brand invested lots of time in proof reading of this thesis and gave me valuable advice for improving it.

I want to thank the entire Hahn research-group and especially the group on tunable materials for the good (working) atmosphere, where everyone supports each other. Thanks to you all it was always really nice to go to work. In particular, I want to thank Philipp Leufke for many helpful discussions as well as LaTeX support whenever it was needed and Christian Reitz for keeping the SQUID alive.

Detlef Schoos has to be mentioned for plenty of helpful discussions regarding the cluster source as well as for providing me the drawings of the TOF.

Finally, I want to thank my whole family, especially my parents, who early awakened my interest in natural sciences, gave me the opportunity to study physics, and support me whenever they can. Moreover I want to thank Charlotte for all her support and love in the exhausting last weeks and months of my thesis work and writing.

Index

Contents

List of Figures

List of Tables

Definition of acronyms and symbols

Acronyms

AFM	Antiferromagnetic/Antiferromagnetism
BCC	Body-Centered Cubic
CAD	Computer-Aided Design
CEMS	Conversion Electron Mössbauer Spectroscopy
CIBD	Cluster Ion Beam Deposition
EB	Exchange Bias
EDX	Energy-Dispersive X-ray Spectroscopy
FC	Field Cooling
FCC	Face-Centered Cubic
FIB	Focused Ion Beam
FM	Ferromagnetic/Ferromagnetism
FWHM	Full Width at Half Maximum
EFTEM	Energy Filtered Transmission Electron Microscopy
HOPG	Highly Oriented Pyrolytic Graphite
IGC	Inert Gas Condensation
MBE	Molecular Beam Epitaxy
MPMS	Magnetic Properties Measurement System
MS	Mössbauer Spectroscopy
PM	Paramagnetic/Paramagnetism
PVD	Physical Vapor Deposition

QCM	Quartz Crystal Microbalance
RT	Room Temperature
SEM	Scanning Electron Microscopy
SPM	Superparamagnetic
SQUID	Superconductive Quantum Interference Device
STEM	Scanning Transmission Electron Microscopy
STM	Scanning Tunneling Microscopy
TEM	Transmission Electron Microscopy
TOF	Time of Flight Mass Spectrometer
UHV	Ultra-High Vacuum
XRD	X-Ray Diffraction
ZFC	Zero-Field Cooling

Symbols

at.%	atomic percent
B_{HF}	hyperfine field
D	film thickness
H_d	nearest neighbor distance
H	magnetic field strength
H_{EB}	exchange bias field
H_C	coercive magnetic field
K_{eff}	effective anisotropy constant
J	exchange integral

M_{sat}	saturation magnetization
μ_0	vacuum permeability
μ_B	Bohr magneton
R	particle radius
T	temperature
T_b	blocking temperature
T_N	Néel temperature
V	particle volume
vol.%	volume percent

1 Introduction

1.1 Motivation

Clusters are generally defined as aggregates of three up to several million atoms or molecules. Clusters, therefore, can be considered as a bridge between atoms and molecules on the one hand, and bulk material on the other hand. In a number of previous studies, especially those conducted on small clusters in the size range of a few nanometers, it was shown that clusters can exhibit novel electronic [1], magnetic [2–5], optical [6] and catalytic [7, 8] properties, that are strongly size dependent and often remarkably different from the properties exhibited by their bulk material counterparts. These new properties result from the high surface to volume ratios (e.g. a cluster with 2 nm diameter consists of roughly 50 % surface atoms) of the clusters, differing them from bulk material of the identical chemical composition. Since the same material in the form of a cluster can display totally new properties, which can be influenced or even fine-tuned by varying the size of the cluster, utilizing clusters as building blocks may lead to new types of materials whose characteristics can be tailored and optimized for the intended applications.

In general, clusters can be synthesized by a variety of chemical and physical methods [9]. A flexible method, in terms of material systems and cluster sizes, offering a high level of control and cleanliness, is the synthesis of the clusters in the gas-phase [3], followed by cluster ion beam deposition (CIBD) in ultra high vacuum (UHV). The range of cluster-composed nanostructures and materials that can be synthesized by CIBD is very broad and it can be grouped in the following four main categories (Fig 1.1):

a. Cluster decorated surfaces: can be considered as the simplest type of cluster-based material. The clusters are either deposited with small energies around the soft landing regime (< 0.5 eV/atom) or somewhat above [10]. In the first case, the deposition energy is well below the binding energy of the clusters, and consequently, during the deposition process, no significant damage is caused on the clusters or on the substrate. In the second case, for slightly higher deposition energies, the clusters induce small defects on the surface of the substrate. In turn, the clusters are directly pinned by these defects,

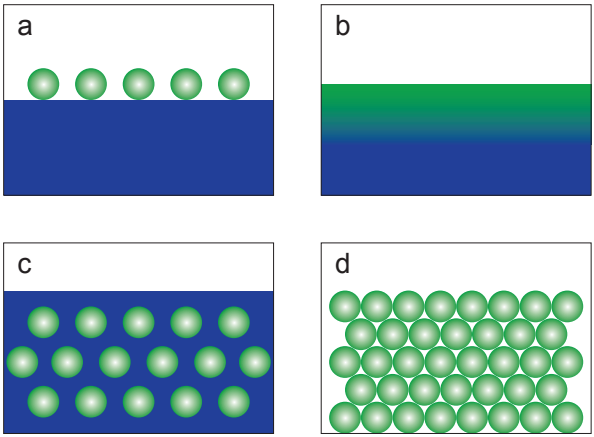

Figure 1.1.: Illustrations of possible cluster-assembled nanostructures and materials: (a) clusters soft-landed on surfaces, e.g. for (nano-)catalysis. (b) Clusters deposited with energetic impact, leading to the creation of surface alloys, e.g. hard coatings. (c) Clusters embedded in a matrix , where the matrix either can act as an inert separation medium, react with the clusters to form an alloy or add an additional functionality. (d) Purely cluster-composed materials.

impeding them from further movement and thus preventing them from agglomerating. Since the clusters reside on the substrate surface, they can easily be studied and examined by microscopic methods, as for example scanning tunneling microscopy (STM). A typical application for this type of material is in the field of (nano)catalysis.

b. Surface alloys: similar to the decorated surfaces (a), except that the deposition energies are considerably higher than those of the decorated surfaces, typically, for small clusters, in the range of several keV per cluster and thus higher than the total binding energy of the clusters. The high impact energy leads to the destruction of the clusters, resulting in the clusters forming a compact, adhering thin film [11].

c. Clusters in matrices: the clusters are typically co-deposited with various types of matrices, from which several benefits can be obtained. First, in the simplest case, the matrix keeps the clusters separated, thus preventing them from agglomerating and sintering. Secondly, the matrix can also add functionality

to the resulting thin film, for example, additional magnetic characteristics. Thirdly, alloys on a local scale can be formed around the embedded clusters if a miscible material combination is used. Furthermore, due to their small radii, in the nanometer range, clusters have high vapor pressures, and, consequently, a high solubility with the surrounding matrix. This promotes the intermixing of the cluster atoms with the surrounding matrix, which might give rise to new types of alloys, among material combinations that are normally immiscible under thermodynamic equilibrium conditions.

d. Purely cluster-composed materials: usually, the deposition of several layers of pure clusters leads to a high degree of sintering and the formation of a bulk-like thin film, without displaying any special characteristics [12]. However, few exceptions exist, which can be put into two main groups. The first group is based on rather stable clusters that keep their shape and structure nearly intact in the resulting bulk material. An example of a material belonging to this group is fullerit, a C_{60} (fullerenes) cluster-based crystal [13]. In the second group are those materials in which interfaces among the deposited clusters are formed; sintering occurs; and, pores that might be left after the deposition process, can be filled with atoms from the clusters. The unique process by which these materials are synthesized, with the clusters being the starting components, this may lead to new material structures, either because the cores of the primary clusters are left after the interface formation and sintering or because new structures are formed at the interfaces among the primary particles.

Generally, depending on the specific application, the clusters being used in all four groups can consist of a single element or an alloy system. Furthermore, the clusters as well as substrates and matrices can be crystalline or amorphous.

Some of the four types of cluster-composed nanostructures and materials can also be synthesized by other methods, than the above-mentioned CIBD. Materials of categories (a) and (d) can, for example, also be prepared by various chemical methods. However, a drawback of these methods has to do with the fact that, chemical synthesis routes, typically, need surfactants. Moreover, through these routes, it is not that straightforward, for example, to synthesize pure metal clusters. In addition, for varying the size of the synthesized clusters, a different synthesis route needs to be used. A material similar to (c), clusters in a matrix, can, in principle, also be synthesized by either co-depositing several immiscible materials or to chemically produce a compound of several materials, in a first step, and then to induce the formation of precipitates in the resulting solid solution, in a second step (e.g. by heat treatment). A clear drawback of such an approach is the lack of

control over the size of the precipitates that are formed as well as the limitation on materials of type (c).

1.2 Experimental requirements

Synthesizing the full range of cluster-based materials in a controlled manner, together with the capability of fine-tuning the properties of the resulting materials, is a very demanding task and, consequently many experimental challenges need to be overcome (see Chap. 2). One key challenge is presented by the naturally high surface to volume ratio of the clusters, making them very susceptible to any kind of contamination, as for example oxidation, that might significantly alter the properties of the clusters. Possibly, the cleanest synthesis route for cluster-based materials, offering also the possibility to size-select the clusters, is the gas-phase synthesis of clusters in an inert atmosphere, followed by CIBD (and other sample processing steps) in UHV. One of the drawbacks of this synthesis route is, that the amounts of clusters that can be produced are typically in the range of micrograms (or even nanograms, if the particles are size-selected). Consequently, the resulting cluster-based samples, are thin films with thicknesses in the micrometer- or nanometer range.

Compared to other thin film deposition techniques, as for example the commonly used physical vapor deposition (PVD) methods such as molecular beam epitaxy (MBE), several additional problems, experimental challenges, and requirements arise for the case of CIBD. Some of these are due to the characteristics (intrinsic nature) of the clusters themselves, while the others originate from the specific type of sample preparation:

Contamination: as already mentioned, a common problem associated with the fabrication of cluster-based materials is the tendency (of the clusters) to react with residual gas molecules due to their high surface to volume ratios.

Size selection: since the properties of the clusters are size-dependent, size selection, prior to their deposition, is one of the fundamental steps that are needed for the synthesis of new materials with tailored properties.

Agglomeration: as the cluster size is critical for the desired properties, rearrangement and/or agglomeration of the clusters after deposition needs to be prevented.

Deposition of well-defined amounts of clusters: the clusters are typically deposited in the form of a rather narrow ion beam with a high lateral intensity gradi-

ent. This complicates (or even prevents) the use of standard film thickness monitors in PVD techniques such as quartz crystal microbalances (QCM), since these sensors require to be placed in an area with rather homogeneous intensity.

Synthesis of homogeneous samples: as previously stated, the cluster beams used in cluster deposition setups are typically narrow, (much sharper than a beam produced, for example, from a thermal source) making the synthesis of homogeneous samples a very challenging task (Chap. 2.4).

Co-deposition of clusters and matrix: for the material type (c) in figure 1.1, a matrix is an essential component and the co-deposition of the clusters with a matrix is beneficial, since the clusters are nearly immediately embedded within the matrix. This has the combined functions of protecting the clusters from oxidation, immobilizing them and, thereby, preventing their aggregation.

Controlled deposition energy: the deposition energy of the clusters is a major factor, that clearly affects the structure and properties of the resulting materials. For example, high impact energies can result in pronounced interface formation or even in the destruction of the clusters during landing (leading to surface alloy formation), while at low impact energies the clusters stay intact and rather loose agglomerates can be formed.

Temperature stabilization of the sample during deposition: since the sample temperature affects the growth of the deposited matrix materials, as well as the mobility of the deposited clusters, the control of the sample temperature, during deposition, is absolutely necessary to achieve reproducible results (see chapter 3.3).

1.3 Scope and outline of this thesis

In order to fulfill the aforementioned requirements, and to find effective solutions for the experimental challenges, an apparatus, dedicated to the fine-tuned synthesis of cluster-based materials, was custom-designed, ion-optically simulated and then constructed. The final product is the CIBD system, which is shown in figure 1.2 and explained in detail in chapter 2. Its key elements are a magnetron sputter/gas aggregation cluster source (producing uncharged as well as ionized clusters), a 90° sector magnet for mass-separation of cluster ions, two complementary deposition stages for sample synthesis, and an ion optical lens system for guiding the

cluster ions from the source to the two deposition stages. The design of the entire system, including vacuum chambers, ion optical elements, sample holders and components, was accomplished using a professional CAD software (Autodesk Inventor Professional). In particular, the final design of the ion optical lens system was accomplished in several iterations of alternately drawing test layouts in the CAD software and the subsequent testing of the layouts in an ion optical simulation software (SimIon). This procedure yielded the final design and, in addition, provided an indication of the voltages needed for the individual electrodes to guide the cluster ions through the apparatus.

The apparatus was tested and its individual elements were optimized by means of a series of experiments, using different types of clusters (amongst others copper, scandium, and iron clusters). The final tests were conducted with iron clusters embedded in a silver matrix and yielded valuable information regarding the capabilities and versatility of the deposition system. The results (published in [14]) clearly demonstrated that the system provides the high degree of control to fulfill all requirements described above for preparing a wide range of materials and morphologies, as shown in figure 1.1. In the literature, such a degree of control has not been previously reported; details and the importance to this and future research, will be presented and discussed in chapter 3.2.

The high degree of control of the deposition parameters made it possible to produce a large series of iron cluster/chromium matrix film samples in a consistent and reproducible manner and thereby enabled to thoroughly investigate the magnetic properties of the material system (Chap. 3.3). Magnetic measurements conducted on these samples yielded insightful results, regarding the magnetic properties of this cluster/matrix system, that, to our knowledge have not been previously reported in the literature.

In recent experiments, the first deposition stage (Fig. 1.2 c, Chap. 2.4.1) was used to synthesize a purely cluster-composed material based on amorphous iron-scandium clusters (Chap. 4). First promising results obtained on these samples suggest the formation of a new type of amorphous structure, displaying magnetic and structural characteristics markedly different from a rapidly quenched alloy of the same chemical composition.

In the following chapters, experiments and results obtained on some of the cluster-composed nanostructures and materials described in figure 1.1 are presented. The content of the individual chapters is described below.

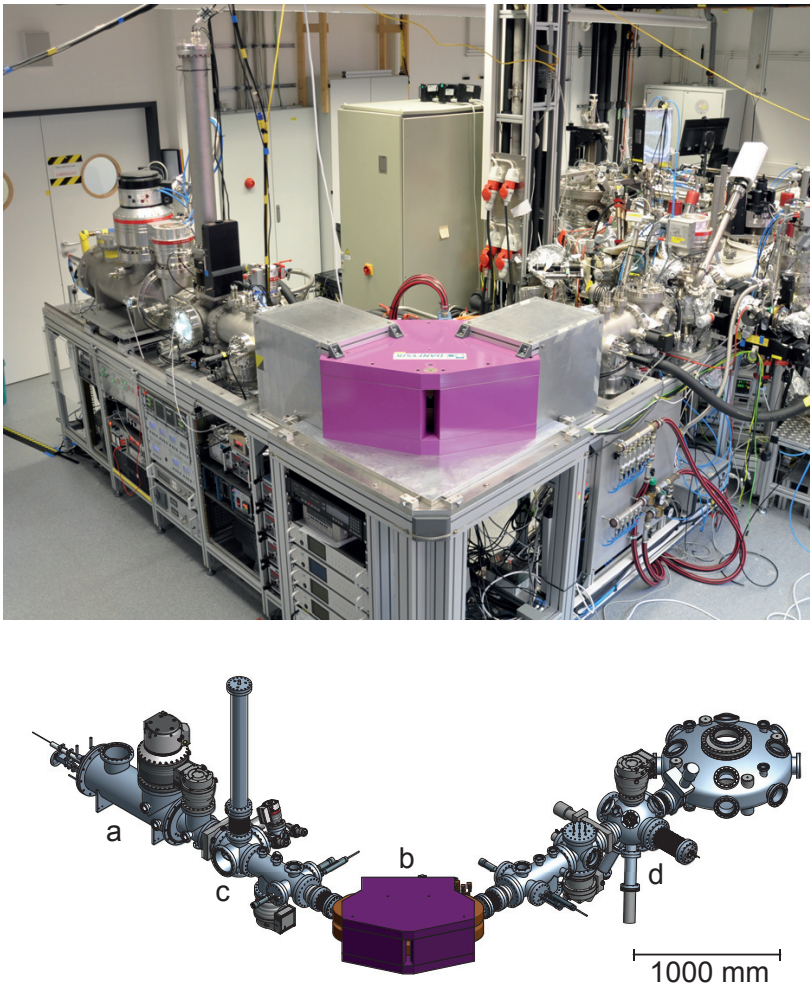

Figure 1.2.: Photograph and computer-aided design (CAD) drawing of the cluster ion beam deposition (CIBD) setup. In the CAD drawing the key elements of the setup are indicated. (a) cluster source, (b) mass separation section with a 90° sector magnet, (c) and (d) deposition stages. Not visible in the drawing is a continuous channel of ion optical elements guiding the cluster ions from the source to the deposition stages.

Chapter 2: Cluster ion beam deposition system. The custom-designed experimental setup for the fine-tuned synthesis of various cluster-composed materials that has been designed, ion optically simulated, constructed, and tested is presented and its key elements are explained in detail in this chapter.

Furthermore, experiments and results obtained on a cluster-composed nanostructure of type (a) in figure 1.1, copper clusters deposited on a highly ordered pyrolytic graphite (HOPG) substrate, are presented. The intention of the experiments was to obtain a confirmation for the size-selection of the clusters as well as to study the influence of the deposition energy on the sample morphology.

Chapter 3: Cluster/matrix nanocomposites: Iron/Silver and Iron/Chromium. In this chapter experiments and results obtained on two materials of type (c) in figure 1.1 are presented, namely iron clusters embedded in a silver matrix and iron clusters embedded in a chromium matrix. Here the focus was to obtain a measure for the capabilities of the CIBD system and to study the magnetic characteristics of the samples in detail.

Chapter 4: A purely cluster-composed material: Iron-Scandium nanoglasses. In this chapter experiments and results obtained on a material of type (d) in figure 1.1, being purely composed of amorphous iron-scandium alloy clusters, are presented. In the experiments the influence of the deposition energy of the clusters on the formation of a novel amorphous state was studied.

2 Cluster ion beam deposition system

Selected parts of this chapter have also been published in [14] within the framework of this thesis. The respective paragraphs – with minor conformations included – are indicated by a vertical gray bar at the inner page margin[1].

In this chapter, the custom-designed experimental setup for the fine-tuned synthesis of cluster-composed materials and its key components are explained in details.

2.1 Motivation and introduction

The synthesis of any type of well-defined cluster-composed material is, in itself, a challenging task, since the majority of the clusters is not chemically inert and the desirable cluster properties may be strongly affected by the presence of impurities (e.g. oxygen). Thus, clean conditions during synthesis are one of the primary requirements in experimenting with cluster-composed materials. Possibly, the cleanest synthesis route is the gas phase synthesis of clusters in an inert atmosphere (i.e. the evaporation of the cluster material combined with gas-aggregation), followed by cluster (ion) beam deposition in UHV. In this synthesis route, the only sources of contamination can be the residual gases in the UHV chamber as well as impurities that might be present in the utilized inert gases and original cluster materials. An intrinsic benefit of CIBD is the possibility to mass-separate ionic clusters, by means of a sector magnet or a quadrupole mass selector. The capability of mass-separation is particularly important for clusters that consist of only a few tens of atoms. Because, in this small-scale regime, one missing or an extra atom can result in significant changes in the cluster geometry [15] as well as affecting the physical and chemical properties of the clusters.

Besides possible contamination, either during synthesis or when exposed to air, clusters tend to agglomerate and thus to form larger aggregates. Except for few cases [12], the unique properties of a single cluster are thereby lost. In the case of surfaces, covered with less than a monolayer of clusters, pinning the clusters to the substrate via impact with defined kinetic energy [16], or deposition on functionalized surfaces is sufficient to keep the clusters separated, thus inhibiting their

[1] *Reprinted with permission from* [14]. ©2015, AIP Publishing LLC.

agglomeration. For unstable clusters or composite systems, co-deposited matrix materials can stabilize and protect the clusters or even add an extra functionality [17] to the resulting cluster/matrix nanomaterial. The stabilizing effect of the matrix may be assisted by cooling the sample down to cryogenic temperatures, during deposition, so as to slow down the movement of the already deposited clusters, until they become covered and protected with matrix material.

Aiming for the synthesis of well-defined and fully tailorable cluster-composed materials, two additional key prerequisites need to be met. Though these prerequisites are standard in conventional PVD techniques, commonly they are are not accounted for in cluster ion-beam deposition studies. These prerequisites are as follows: (1) the ability to precisely control the deposited amounts of material (clusters); (2) the ability to synthesize homogeneous samples with a uniform cluster coverage. Due to the particular beam characteristics in a CIBD system it is not a trivial task to fulfill both requirements. The cluster ion beam has a rather narrow (compared to standard evaporation sources) Gaussian-like intensity profile that is strongly dependent on both, the source and electrode settings, which makes uniform coverage as well as monitoring the particle flux on the sample quite challenging. The importance of this aspect is demonstrated in chapter 3.2 using an assembly of superparamagnetic clusters (in a matrix) whose magnetic characteristics are strongly influenced by the average cluster–cluster distance.

In this chapter a new cluster ion beam line that has been designed and constructed for the fine-tuned synthesis of diverse cluster-composed nanostructures and materials is presented. The main focus was to gain as much control as possible over the critical sample characteristics such as the cluster size and cluster amounts (and sample homogeneity) as well as a high degree of sample purity. The system is capable of producing a wide range of particle sizes, from a single atom up to several thousand atoms per cluster, providing a cluster beam with a narrow mass distribution of about 2 % to 10 %. The synthesis system is equipped with two deposition stages, the first directly utilizing the full cluster ion beam leaving the source, and yielding micrograms of clusters within a few hours (Sec. 2.4.1), whereas by means of the second stage nanograms of mass-separated clusters (deposition time typically a few hours) can be co-deposited with chosen matrix materials (Sec. 2.4.2). The centerpiece of both deposition stages is a custom-designed sample holder/mask combination (Sec. 2.4). As shown in chapter 3.2, this combination allows for precisely controlling the amount of deposited clusters on a sample (±10 %), and also obtaining a homogeneous sample coverage (±10 %). This high degree of precision makes it possible to produce consistent series of samples with small increments in cluster size and cluster amount in the matrix, which enables detailed investi-

gations of various cluster-composed materials (e.g. the extensive Fe_x/Cr sample series whose properties are presented in chapter 3.3).

To ensure as clean as possible deposition conditions, turbo pumps with a combined nominal pumping speed of 4200 l/s were installed on the vacuum system, keeping the pressure in the second deposition stage in the mid 10^{-9} mbar range, during operation of the system.

A schematic of the apparatus, comprising all functional sections, is shown in Fig. 2.1. The clusters are produced in a magnetron sputtering/gas aggregation cluster source [18], (Sec. 2.2, Fig. 2.1 a) and then extracted in a supersonic expansion by the aggregation (He) and sputtering gases (Ar), respectively. Either anions or cations (the source produces anions, cations and neutrals) are further accelerated by a set of electrostatic lenses (Fig. 2.1 b) to form an ion beam, with the beam energy encompassing a range of 0.1 to 1 keV. In the next section of the apparatus the clusters can be directly deposited in the first deposition stage (Fig. 2.1 c, Sec. 2.4.1), and their mass distribution can be analyzed by means of a transverse Wiley-MacLaren-type time of flight mass spectrometer [19] (TOF, Fig. 2.1 d, Sec. 2.5). Alternatively, the clusters can be further transferred into the mass separation section (Sec. 2.3). Clusters entering the mass separator pass through an electrostatic quadrupole triplet (Fig. 2.1 e) to be focused into the entrance slit of a 90° sector magnet (Fig. 2.1 f), followed by an exit slit and a second quadrupole triplet. Finally, continuing in straight path, the clusters enter the deposition chamber onto a second deposition stage (Fig. 2.1 g, Sec. 2.4.2).

In the following sections, the essential parts of the apparatus are described in more details.

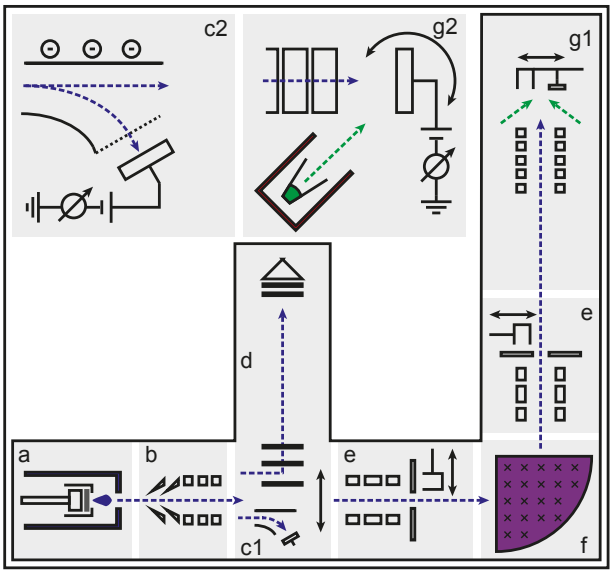

Figure 2.1.: Schematic of the cluster ion beam deposition (CIBD) system. (a) Cluster source. (b) Differential pumping and acceleration lenses. (c1) Sample holder for deposition of as-prepared clusters. (d) Transverse time of flight mass spectrometer (TOF). (e) Quadrupole triplet, selection slit and Faraday cup detector. (f) 90° sector magnet. (g1) Deposition chamber with deceleration lenses, sample holder, Faraday cup and evaporation sources (green). (c2) Detailed view of (c1). (g2) Detailed view of (g1).

2.2 Cluster source

The cluster source (Fig. 2.2) is based on the well-known design of Haberland et al. [18], utilizing magnetron sputtering in combination with inert gas condensation. In order to merge these two processes a magnetron sputter head (Fig. 2.2 a) is mounted in a liquid nitrogen cooled tube (Fig. 2.2 b), and immersed in a He stream (Fig. 2.2 c). Ar is used as sputtering gas (Fig. 2.2 d), and the sputtered atoms are cooled down via collisions with the cool He and Ar atoms to aggregate to clusters of various sizes. At the end of the cooled aggregation region (Fig. 2.2 e) the clusters leave the source through an adjustable iris (diameter 1 to 15 mm) in a supersonic expansion (Fig. 2.2 f), which effectively stops cluster growth. The cluster size is thereby mainly determined by the ratio of the Ar and He flow rates

(typically 100 sccm of Ar and up to 800 sccm of He), and can be further fine-tuned by means of the aggregation length (distance between the sputter head and the iris, typically 5 to 20 cm), the pressure in the aggregation region (0.1 to 10 mbar, adjusted by the opening of the iris) and the magnetron sputtering power (typically 20 to 100 W).

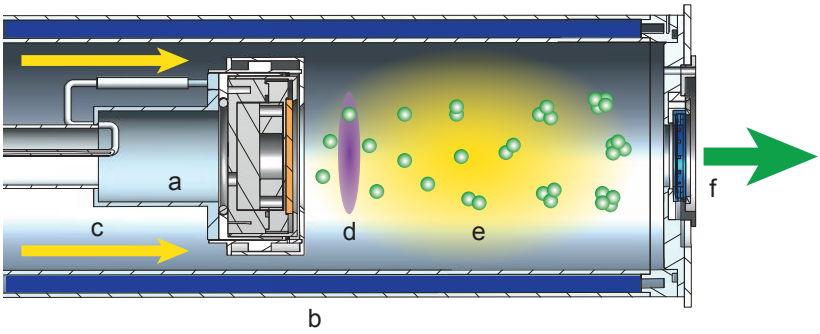

Figure 2.2.: Computer-aided design (CAD) drawing of the cluster source. The magnetron sputter head (a) is placed in a liquid nitrogen cooled tube (b) and immersed in a He stream (c). Ar is used as sputtering gas (d). The sputtered atoms condense to clusters in the aggregation zone in front of the sputter head (e) and leave the source in a supersonic expansion with He and Ar through an adjustable iris (f).

Figure 2.3 shows typical mass distributions in a cluster beam produced by the sputtering source using a Cu sputtering target. In example (a), the source was adjusted to produce large negatively charged Cu clusters and the maximum of the mass distribution was shifted from clusters with 500 atoms to clusters with 3000 atoms, by changing the He flow rate from 210 to 70 sccm. All other parameters were kept constant (e.g. source parameters, electrode voltages).

Example (b) shows the opposite side of the accessible mass range of the cluster source by means of small positively charged Cu clusters. In general, small clusters are, to a great extend, positively charged, which might be due to the fact that capturing an extra electron during the gas aggregation process is unlikely for small particles, in which the extra electron would have to be accommodated by few atoms in a small volume. On the left side (small masses) of the mass spectrum (b) many additional mass peaks are visible. These peaks can be assigned to various types of $Cu_xAr_xHe_x$ clusters and are not present anymore for cluster size larger than Cu_{14}.

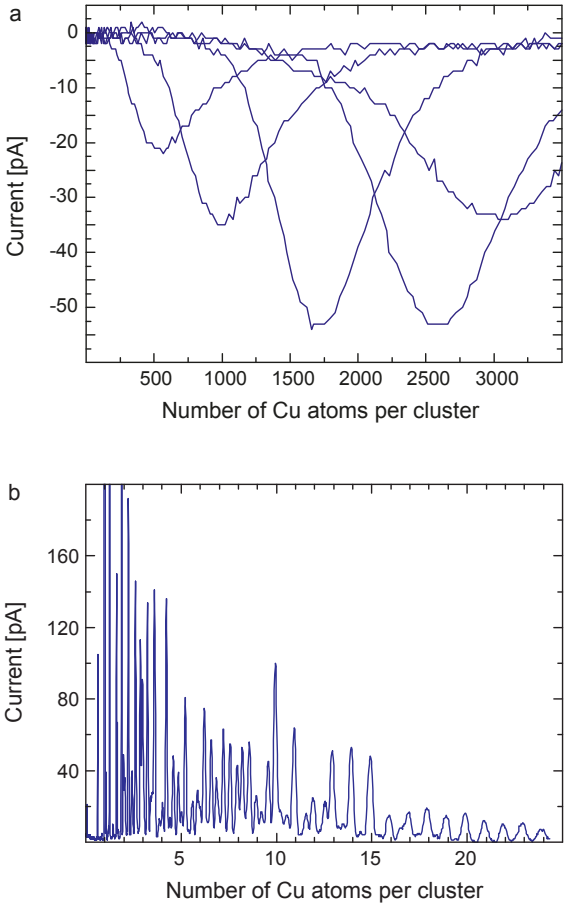

Figure 2.3.: Representative mass spectra of Cu clusters recorded at the second deposition stage by scanning the magnetic field of the sector magnet. (a) Large negative Cu clusters in the primary beam prior to mass selection, recorded with 110 sccm Ar and different He flow rates. All other parameters were kept constant. From left to right: 210 sccm He, 150 sccm He, 110 sccm He, 90 sccm He and 70 sccm He. (b) Small positive Cu clusters. In the size range of a few Cu atoms/cluster (left part of the mass spectrum) additional peaks belonging to $Cu_xAr_xHe_x$ clusters are visible. Starting from Cu_{14} just pure Cu clusters are left.

In general, among the clusters leaving the source, roughly 50 % are neutral, while the other 50 % are ionized [18]. The relative amounts of neutral to ionized clusters can vary, depending on the material used. Based on experimental observations, the cluster ions are singly charged, a second mass distribution suggesting doubly charged clusters has, has not been observed. For the deposition experiments only ionic clusters are utilized, since the charge allows for analysis, mass separation, and further manipulation of the clusters.

2.3 Electrode system & mass separation

The mass separation section is based on a sector magnet, which is, in fact, not only a mass but also an energy selector. Hence, in order to achieve a high mass resolution, it is essential to reduce the ratio of the width of the kinetic energy distribution of the cluster beam and its kinetic energy ($\triangle E_{\mathrm{kin}}/E_{\mathrm{kin}}$). The energy width of a single cluster species in the beam ($\approx 5\,\mathrm{eV}$) is primarily caused by the source itself and cannot be reduced without applying a disproportionately great effort. Therefore, it is advantageous for the optimal mass resolution, if the clusters pass the magnet with the highest possible kinetic energy, which in turn is ultimately limited by the ability of the magnet to deflect the clusters (the maximum magnetic field available).

The cluster source is at ground potential (changing the source potential is possible, but not easy, since that would require modifications of both the magnetron power supply and the source design) and the clusters are initially accelerated only by the expansion of the sputtering and aggregation gases. Therefore the resulting cluster kinetic energy is of the order of a few eV, which is only marginally higher than the typical energy width of the cluster ion beam, being neither sufficient to form an ion beam without too many losses, nor for useful mass separation. In order to reach higher beam energies, the clusters are therefore accelerated by the acceleration lenses to a "base energy" in the range 100 eV to 1000 eV and enter a continuous channel of electrodes guiding them all the way through the apparatus. A portion of these electrodes is thereby used for specific tasks such as the steering or focusing of the cluster ion beam, while the remaining portion is used to preserve the base potential and to shield the ions from ground.

Figure 2.4 shows an example of the electric potential versus distance curve in the apparatus and the continuous channel of guiding electrodes. The source (Fig. 2.4 a) is at ground potential (V_{Source}) and is followed by the acceleration lenses, where the potential is step-wise increased up to the "base potential" (V_{Base}), with a maximum of 1000 V (1 keV cluster ion energy). In the mass separation section (Fig. 2.4 b, Fig. 2.6), the clusters are kept at that potential except for adjustments in the

quadrupole triplets for focusing purposes. The quadrupole triplet in front of the magnet (Fig. 2.5) is thereby used to prepare the cluster ion beam for mass separation and the second triplet, downstream of the magnet, to recover the initial circular cross-section of the beam. In detail the first quadrupole (Fig. 2.5 a) of the first triplet is used to aim the beam onto the entrance slit of the magnet, located 500 mm in front of the magnet at its image point (Fig. 2.5 d). Using the second quadrupole, the cluster ion beam is focused in the horizontal plane into the entrance slit, while with the third quadrupole (Fig. 2.5 c) it is focused in vertical direction into the center of the magnet, being the optimal setting minimizing the losses at the walls of the shallow vacuum chamber in the pole gap of the magnet. Behind the mass separation section, approaching the end of the apparatus (Fig. 2.4 c), the mass-separated clusters are step-wise decelerated and refocused by a series of six cylindrical electrodes to finally be deposited with an adjustable energy.

Figure 2.6 a shows a CAD drawing of the mass separation section. It starts from the left with the first quadrupole triplet, which is then followed by the entrance slit. In the center is the vacuum chamber inside the magnet and at the end (the right side) the exit slit and the second quadrupole triplet are located. An ion optical simulation, using SimIon, of the same arrangement (except for electrodes keeping the base potential) is shown in Fig. 2.6 b. The simulated ion beam contains Fe_{19}, Fe_{20} and Fe_{21} with an energy of 1000(10) eV and a beam spot size of 6 mm being, according to experience, realistic parameters for this type of ion beam. In the simulation the quadrupole voltages were optimized, as previously described, and the magnetic field was set to guide Fe_{20} through the exit slit. In the detailed view of the exit slit and the second quadrupole triplet (Fig. 2.6 c) it becomes clear that Fe_{20} is completely separated from the other two cluster sizes, and Fe_{20} is the only species to pass the exit slit. The maximum mass separation with these settings is clearly higher than 1/20, since the trajectories of the Fe_{19} and Fe_{21} ions are not even close to the slit.

Since the bending magnet is a critical component and, at the same time, is the limiting factor for the mass resolution, a large 90° sector magnet with a radius of 500 mm, a pole gap of 22 mm (inner vacuum tube height 18 mm), and a maximum magnetic field of $\mu_0 H = 1.4\,\mathrm{T}$ (custom-made, Danfysik) was chosen as the key element of the mass separation unit. These specifications result in a mass-energy-product of 23.6 MeV amu (i.e. particles with an energy of 1 keV and a mass less than 23600 amu can still be deflected by the magnet). Therefore, the upper mass limit is defined by the lowest reasonable beam energy (around 50 to 100 eV) resulting in approximately 400000 amu. Assuming a beam spot size of less than 1 cm, at the image point (position of the entrance slit) and a beam energy of 1 keV, the dimensions

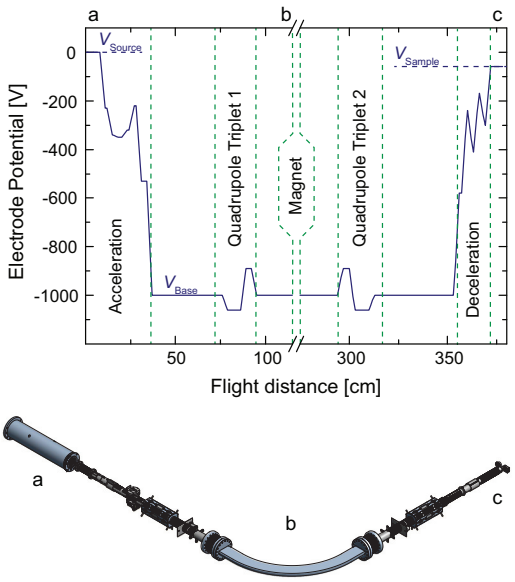

Figure 2.4.: Top: example for the electric potential versus distance curve in the apparatus. Bottom: computer-aided design (CAD) drawing of the electrode channel guiding the ions through the apparatus. The source (a) is on ground potential. It is followed by an acceleration region, where the electrode voltages are increased in order to accelerate the clusters to gain kinetic energy for mass separation (b). At the end of the apparatus, approaching the second sample holder (c) the clusters are finally decelerated to reach the deposition energy.

of the magnet yield a theoretical maximum mass resolution of 1/50. However, during an actual experiment, lower resolutions of 1/10 to 1/40 are achieved due to the lower beam energies needed for large clusters and the energy width of the cluster beam.

To control the mass separation process, a precise measurement of the applied magnetic field and the particle energy is of critical importance. To this end, the magnetic field inside the magnet is continuously monitored by a Tesla meter (GROUP3, DTM-133-PS), while the kinetic energy of the clusters is measured in Faraday cup detectors, equipped with retarding grids (Sec. 2.5).

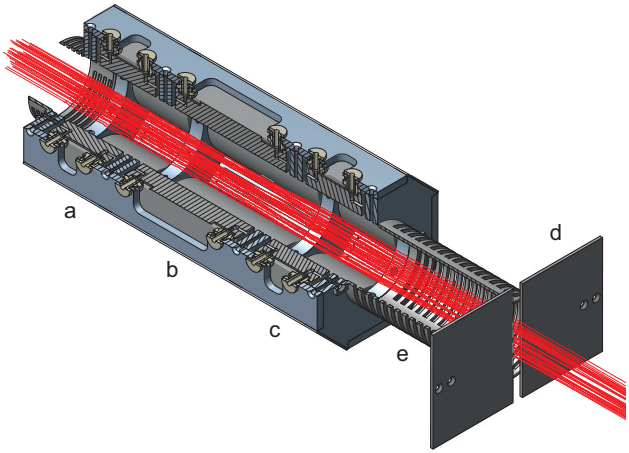

Figure 2.5.: Computer-aided design (CAD) drawing of the first quadrupole triplet with simulated ion trajectories. (a) First quadrupole, used for steering the cluster ion beam and aiming on the selector slit (d). (b) Second quadrupole, used for focusing the cluster ion beam in the horizontal plane onto the entrance slit. (c) Third quadrupole, used for focusing the cluster ion beam in the vertical plane into the center of the magnet for minimal losses. (e) Guiding channel electrode keeping the base potential.

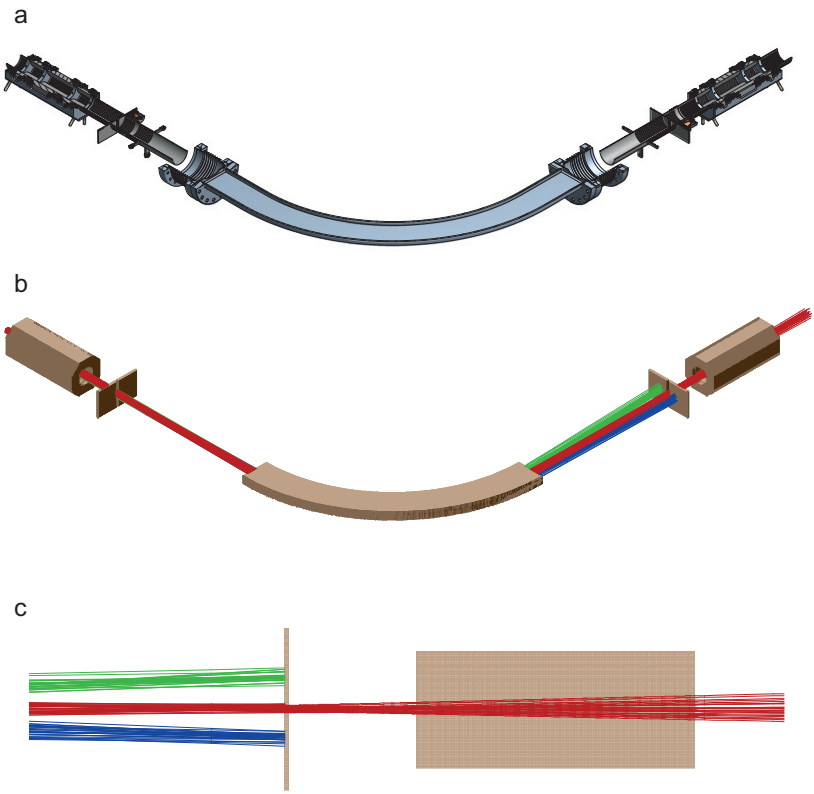

Figure 2.6.: Mass separation section of the apparatus. (a) Computer-aided design (CAD) drawing showing the two quadrupole triplets in front and behind of the magnet, respectively, and the ultra-high vacuum (UHV) chamber in the magnet which is part of the continuous channel guiding the clusters through the apparatus. (b) Ion optical simulation of the ion optical elements of the mass separation section extracted from SimIon (only focusing electrodes are shown). The simulated ion trajectories belong to Fe_{19} (green), Fe_{20} (red) and Fe_{21} (blue) with realistic beam characteristics of 1000(10) eV beam energy and a beam spot size of 6 mm. (c) Detailed view of the exit slit of the magnet and the second quadrupole triplet showing that the three cluster sizes are clearly separated from each other.

2.4 Cluster deposition

As already mentioned in the introductory part, several problems need to be solved for the successful synthesis of well-defined cluster-composed materials by CIBD. Amongst others:

1. deposition on a defined sample area
2. synthesis of uniform samples
3. deposition of defined amounts of material (clusters)
4. deposition of matrices.

(1.) With PVD techniques (e.g. MBE), deposition on a specific area, is typically achieved by placing a mask in front of the sample that has the function of covering parts of the substrate where no material is to be deposited. The same procedure and masks used for PVD techniques can also be used in CIBD.

(2.) Since the generated atomic beams in PVD techniques have a wide opening angle, large uniformly coated areas can be produced. In contrast, however, in CIBD systems, the cluster beam has a typically narrow Gaussian beam shape. Therefore, with the ion beam system, uniform sample coverages can only be obtained by continuously sweeping the cluster beam over the sample with scanning electrodes and restricting the sample area to the central part of the sweeping range.

(3.) In most PVD techniques the amount of deposited material can be easily monitored by means of a QCM, which is positioned close to the sample. The ratio between the amount of material deposited on the QCM and the sample is thereby constant over a long period of time. In contrast, the narrow Gaussian shape of a cluster ion beam is strongly influenced (with respect to the beam center, shape, and width) by the electrode and source settings. Thus, each adjustment in the apparatus, for example, changing the voltage of a single electrode, as it is done frequently, would require a new calibration of the QCM. Thus, an alternative approach is needed. A promising way is to count impinging charges on the sample with a picoamperemeter. Assuming one charge per cluster, which is to a great extend valid for the case of a Haberland-type cluster source, and a well-known cluster size distribution, the amount of deposited material can be closely monitored. This requires to exclusively count the clusters that in fact hit the sample, while at the same time, ignore clusters that hit the surrounding masks, electrodes or the sample holder. This important requirement was realized by electrically insulating the

sample from the mask and grounding of the sample itself via the picoamperemeter.

(4.) When clusters and matrix materials are co-deposited an additional problem arises due to the fact that matrix material and clusters are usually deposited from different directions. Therefore, shadowing effects, due to the finite thickness of the mask, can occur. This, in turn, will result in small areas of the sample containing pure clusters without any matrix or protective material. A possible way to overcome this problem is to move the mask slightly away from the substrate, just far enough to allow the matrix material (deposited from a different direction) to pass the mask, and thereby to cover a larger area than that containing the clusters.

To address all of the four mentioned problems discussed above, a special combination of a sample holder and mask was developed. It is shown in Fig. 2.7.

The sample holder/mask arrangement is based on a standard sample holder (Omicron) that is equipped with a custom-made mask. The mask (Fig. 2.7 b1) is insulated from both, the sample and sample holder (Fig. 2.7 b3) by a thin ceramic plate (Fig. 2.7 b2, red) and it is grounded via a battery pack or high voltage power supply. The substrate (yellow) is in contact to the sample holder and grounded via a battery pack and a picoamperemeter. In this configuration only clusters (purple) passing the mask and hitting the sample behind are counted and at the same time the deposition area is defined and restricted by the opening of the mask. This way, the amount of deposited material (clusters) per area can be monitored. The matrix material (green), which is deposited under an incident angle of 70° (Sec. 2.4.2), passes the mask via a second opening on the side of the mask. Therefore, the matrix material can cover a larger area than the clusters and no shadowing effects can occur. Figure 2.7 c shows a sample composed of Fe clusters that are embedded in an Ag matrix. The cluster deposition area on the sample (purple), is completely embedded in the Ag matrix deposition area (green).

As already mentioned in the introduction, two complementary stages are available for cluster deposition. The first stage being located close to the source, allows for the deposition of large amounts of as-prepared clusters without mass-selection. The second one is located at the far end of the apparatus, offering the possibility to co-deposit mass-selected clusters and matrix materials. The previously described, custom-build sample holder can be inserted in both stages.

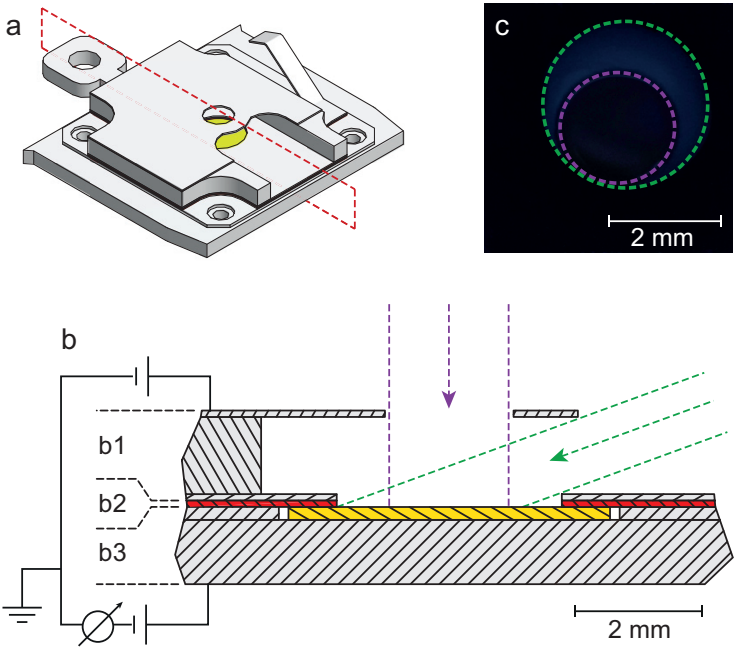

Figure 2.7.: (a) Standard sample holder (Omicron) with custom-made mask for deposition of defined matrix / cluster samples. (b) Sectional view of the sample holder and the mask. The mask (b1) is insulated from substrate/sample (yellow) and sample holder (b3) via a thin ceramic layer (b2). The clusters (purple) pass the mask through the central hole. After deposition on the substrate they are completely covered by the matrix material passing the mask from the side (green). (c) Photograph of an Fe cluster/Ag matrix sample on a silicon substrate. The Fe cluster spot (purple) is centered on the silicon substrate and completely embedded in the Ag matrix spot (green).

2.4.1 Deposition of as-prepared clusters

Using the first deposition stage (Fig. 2.1 c), it is possible to synthesize purely cluster-composed thin films with thicknesses of several hundred nanometers, corresponding to masses in the microgram range. This amount of clusters is sufficient for a large variety of experiments such as, amongst others, mechanical tests and various spectroscopic methods.

In this deposition stage the clusters are deposited in the as-prepared condition, exhibiting the natural mass distribution produced by the source (cf. Fig. 2.3). In the case of cluster ions, the final cluster size distribution is thereby adjustable by the source settings and monitored by the TOF. As indicated in Fig. 2.1 the TOF and the deposition stage are both mounted on a manipulator. This allows to move either the extraction and acceleration plates of the TOF into the cluster beam or the deposition stage. Therefore, the extraction region of the TOF can be placed in the same position as the deposition stage and the monitored cluster size distribution will match the one of the deposited clusters.

Figure 2.8 shows a sectional view of the deposition stage and simulated ion trajectories extracted from SimIon. The stage is equipped with two sample mounts into which the modified sample holders (yellow) can be mounted. One of the sample mounts faces the source directly (Fig. 2.8 a), allowing one to deposit the full cluster beam including neutrals. The second mount (Fig. 2.8 b) has been designed and optimized for the deposition of ionized clusters. To avoid neutral clusters to reach the sample, this mount is placed on an off-axis position with respect of the cluster beam direction, and the ionized clusters are guided to the sample mount by a deflection electrode (Fig. 2.8 c), that can also be used to sweep the beam over the sample to achieve a uniform sample coverage. As previously described, the amount of deposited clusters on the sample can thereby be monitored by a picoamperemeter (Keithley 6485).

In addition, during the deposition, the impact energy per cluster can be set in a range from 10 eV to 12 keV by means of an applied voltage on the sample mount to achieve different cluster landing conditions, ranging from soft landing up to energetic impact.

After cluster deposition, the samples can be transferred into a neighboring UHV chamber where a protective layer can be added by a thermal evaporator.

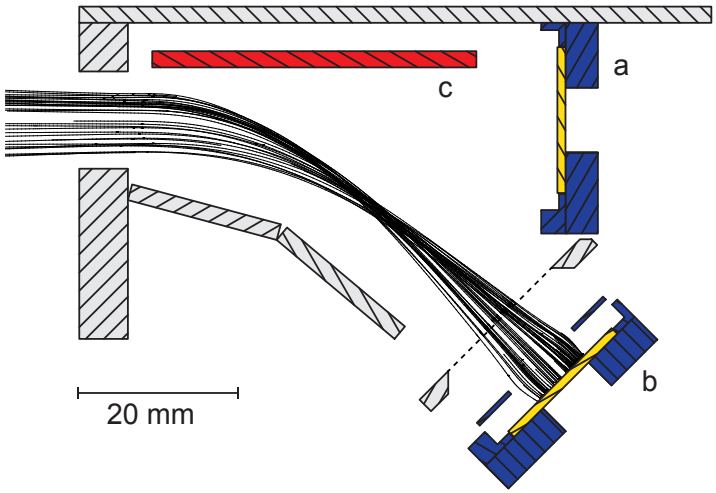

Figure 2.8.: Sectional view of the first deposition stage with simulated exemplary ion trajectories extracted from SimIon. The deposition stage has two sample mounts (blue) for the modified Omicron sample holders (yellow, Fig. 2.7): (a) for deposition of the full beam (including neutrals) and (b) for deposition of ionized clusters. The ionized cluster are guided to (b) by a deflection electrode (c). The simulation was performed with an ion energy of 500(10) eV, a cluster size of 1000 Fe atoms/cluster (56000 amu) and a deposition energy of 100(10) eV. The required deflection voltage was 280 V.

2.4.2 Deposition of size-selected clusters

The second deposition stage, located behind the mass separation section at the end of the apparatus, is dedicated to the deposition of defined amounts of mass-selected clusters with the option of co-depositing matrix materials under UHV conditions. The base pressure in the deposition region is in the low 10^{-10} mbar range and it remains in the 10^{-9} mbar range during operation. Depending on the cluster size and the selected material, a cluster film thickness in the range of 10 nm (purely composed of clusters) can be obtained. This corresponds to nanograms of pure clusters. During the deposition, the sample mount can be cooled down to 153 K as well as heated to up to 673 K.

Figure 2.9 a provides an overview of the second deposition stage and Fig. 2.9 b shows a sectional view of the stage (the area marked with the dotted red square).

In the sectional view in addition simulated ion trajectories extracted from SimIon are shown. The clusters coming from the mass separation section of the apparatus (Sec. 2.3), are guided to the sample mount by means of a set of cylindrical electrostatic lenses (Fig. 2.9 b1) for focusing and for decelerating or accelerating the clusters. The last electrode in front of the sample mount (Fig. 2.9 b3) is a four-sector electrode (Fig. 2.9 b2), that can be used to sweep the cluster beam over the sample. The exemplarily simulated cluster ion trajectories show an undisturbed ion beam which is focused on the sample (black ion trajectories) and an ion beam being deflected upwards when ± 6 V is applied on the upper and lower electrodes of the four-sector electrode (grey ion trajectories).

The sample mount is placed on a rotational platform, allowing for rotation of the sample by nearly 360°. Therefore, the sample can be set to face the cluster beam as well as two evaporation sources, a high temperature effusion cell (CreaTec Fischer & Co., HTC) and a mini e-beam evaporator (Focus GmbH, EFM 3). During cluster deposition, both evaporators face the sample holder at an incident angle of 70° (Fig. 2.9 b4). As described in Sec. 2.4, in such an arrangement, co-deposition of cluster and matrix materials using both sources is possible. As in the case of the first deposition stage (previously described), the cluster ions reaching the sample are continuously counted with a picoamperemeter (Keithley 6485).

Owing to the option for controlled sweeping of the cluster ion beam over the sample with the four-sector electrode, in combination with the special sample holder/mask design, it is possible to produce homogeneous samples with defined cluster film thicknesses. This capability of the deposition system was clearly demonstrated with experiments on Fe cluster/Ag matrix samples (Chap. 3.2). Figure 2.10 a shows a typical intensity profile of the cluster beam. It was recorded with the third Faraday cup, placed at the position of the second deposition stage, through a 0.5 mm aperture. The full width at half maximum (FWHM) is smaller than 2 mm and thus, making it impossible to produce homogeneous samples. Figure 2.10 b shows a simulated intensity profile, assuming that the cluster beam is scanned over the sample surface with the four-sector electrode (± 1 V in x and y direction respectively). In the simulated case, the FWHM is much larger and the resulting sample would, consequently be more homogeneous. The homogeneity of the sample can be enhanced even further by continuously sweeping the cluster beam over the whole sample surface.

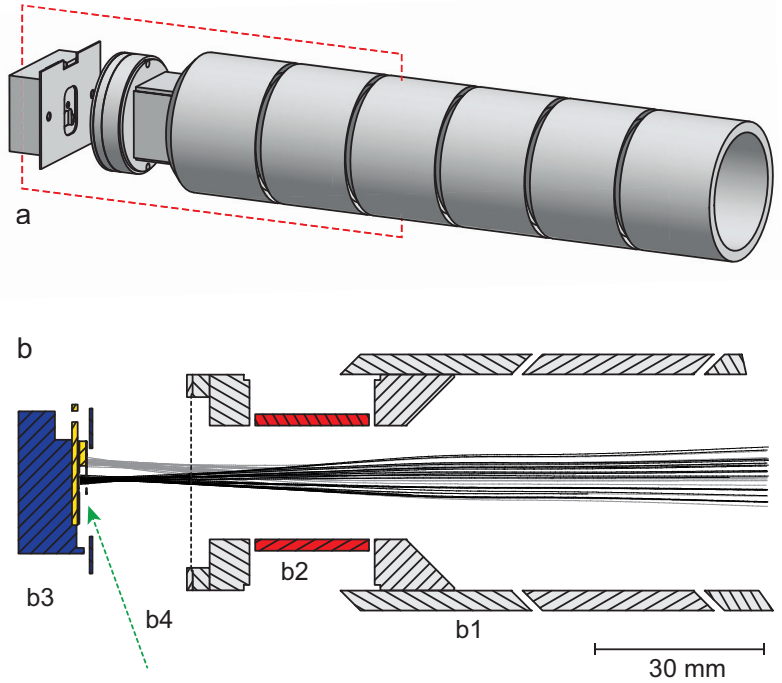

Figure 2.9.: (a) Overview of the second deposition stage. (b) Sectional view of the second deposition stage with simulated ion trajectories. The clusters (black trajectories) pass electrostatic lenses for deceleration and focusing (b1), can be deflected in a four-sector electrode (b2, grey trajectories) and deposited on the sample holder (b3). Matrix material (b4) is deposited under an incident angle of 70°. For the simulation an ion energy of 500(10) eV, a cluster size of 1000 Fe atoms/cluster (56000 amu) and a deposition energy of 50(10) eV were used. The grey cluster beam was deflected with ± 6 V on the four-sector electrode.

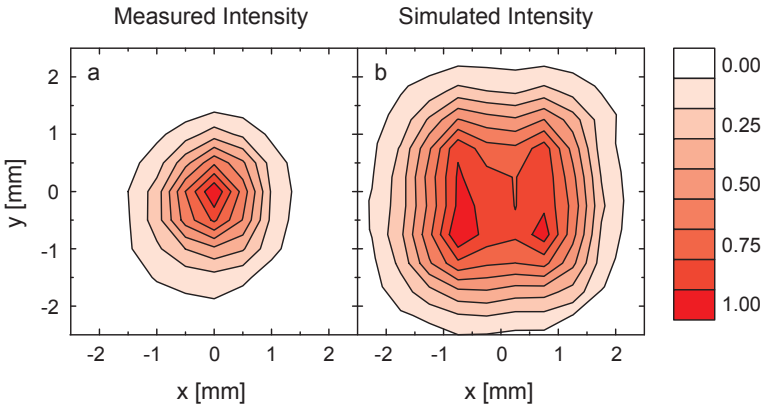

Figure 2.10.: (a) Intensity profile of the cluster ion beam close to the second deposition stage. It was measured with the third Faraday cup equipped with a 0.5 mm aperture. (b) Simulated intensity profile on the sample resulting from scanning the beam with the four-sector electrode in front of the second sample holder by $\pm$ 1 V in x and $\pm$ 1 V in y-direction respectively. It demonstrates, that the uniformly covered area on the sample can be enlarged by sweeping the beam over the sample.

2.5 Beam detection & analysis

In addition to the magnet and the TOF, for beam detection and analysis purposes three Faraday cups (Fig. 2.11) are available in the cluster deposition system.

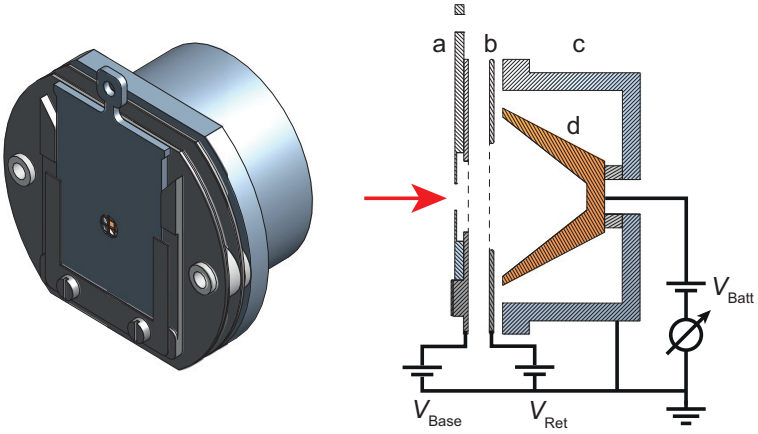

Figure 2.11.: Computer-aided design (CAD) drawing of a Faraday cup. In the sectional view the different parts are visible: (a) *in-situ* exchangeable aperture (diameter 0.5 to 10 mm) with a grid, kept at V_{Base}. (b) Retarding grid for recording energy spectra of the cluster ion beam (V_{Ret} = -50...+50 V). (c) outer cup, at ground potential to shield the inner cup (d), which is grounded via a battery pack (57 V) and a picoamperemeter for current read-out.

Being positioned in front and behind of the magnet (Fig. 2.1 e) and at the last sample holder (Fig. 2.1 g), the Faraday cups allow for step by step optimization of the electrode settings throughout the apparatus. In order to measure the exact beam energy as well as the energy width of the cluster beam, all three cups are equipped with retarding grids: the energy distribution of the cluster ion beam can be determined by recording the ion beam current with respect to the retarding voltage.

The TOF is a transverse Wiley-MacLaren-type and has a two stage extraction and acceleration unit. As shown in figure 2.1 d and described in section 2.4, the extraction unit is mounted on a manipulator, which allows to move it into the cluster beam as well as to exchange it with the first deposition stage (Sec. 2.4.1). Its flight tube length is 1100 mm and a maximum transverse acceleration voltage of 6.5 kV can be applied via two high voltage pulsers (Behlke, GHTS 60). As detector, a two

plate microchannel plate detector, in chevron configuration with a 50 Ω matched conical anode, is used.

The TOF allows for quick tuning of all relevant source parameters and due to its resolution of roughly 1/200 it also detects impurities (e.g. O) in the clusters. Figure 2.12 shows two representative mass spectra of Sc cluster cations recorded at identical source settings. The blue spectrum was recorded shortly after venting and cleaning the cluster source. It shows additional mass peaks between the pure Sc clusters, which are mainly due to Sc_xO clusters (plus some light $Sc_xAr_xHe_x$ clusters). These peaks, related to oxidized clusters, vanished after some hours of source operation (green spectrum).

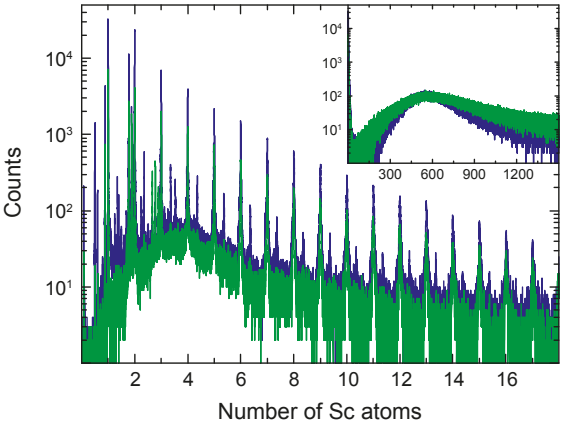

Figure 2.12.: Representative mass spectra of positive Sc clusters recorded with the time of flight mass spectrometer (TOF). The main graph shows the small clusters and the inset the entire mass distribution. In the blue spectrum (plotted behind the green spectrum) additional peaks between the Sc clusters are visible, that can be assigned to singly oxidized Sc_xO clusters.

The above example underlines the important role of the TOF as a valuable too to ensure the purity of the clusters and also shows the importance of recording mass spectra prior to sample synthesis.

2.6 Integrated UHV facility

The cluster deposition system is part of a large integrated UHV facility (base pressure low 10^{-9} mbar) with *in-situ* access to various UHV sample preparation and analysis instruments, that allow for the deposition of additional layers on the cluster samples, as well as the direct analysis of the as-prepared samples. The entire system includes two MBE systems, a sputtering system, a sample preparation chamber (annealing, O and Ar plasma guns), an X-ray/ultraviolet photoelectron spectroscopy system (XPS/UPS, Specs), an Auger electron spectroscopy system (Specs) and an AFM/STM (Omicron).

2.7 Deposition tests

In order to perform initial tests of the CIBD system, the simplest configuration (Fig. 1.1 a) was selected and Cu clusters were deposited on HOPG substrates. Besides demonstrating the successful deposition of isolated clusters on a substrate, including the variation of the deposition energy, such systems can be of interest for tests of the catalytic properties of clusters.

In Fig. 2.13 STM images of deposited Cu_{100} and Cu_{2000} clusters are shown. The Cu_{100} clusters were deposited with an energy of 4 keV per cluster, well above the soft landing regime. The high impact energy of the clusters resulted in the creation of surface defects and subsequent pinning of the clusters to these defects. Therefore, no visible aggregation at steps of the HOPG occurred even several days after deposition and single clusters are still visible in the image. In contrast, the Cu_{2000} clusters were soft-landed with just 1 keV per cluster, corresponding to $\approx$0.5 eV/atom, which is not sufficient to create defects in the surface of the HOPG. Hence, the clusters remain mobile on the surface and form large aggregates.

In order to verify the size of the deposited clusters (in addition to the mass-adjustment performed in the sector magnet), a high resolution STM image was taken of one of the Cu_{100} clusters (Fig. 2.14). The corresponding cross-section indicates a lateral size of 3.5 nm and a height of 0.6 nm. However, assuming the normal Cu density and a spherical cluster, one would expect a diameter of 1.2 nm. This apparent discrepancy might be explained by the high impact energy, which can lead to the partial burying and deformation of the clusters as well as the finite STM-tip size resulting in an overestimation of the lateral cluster size. Therefore, the real cluster diameter can be expected to fall in the range between 0.6 nm and 3.5 nm, which is consistent with the calculated 1.2 nm diameter expected for the non-deformed clusters.

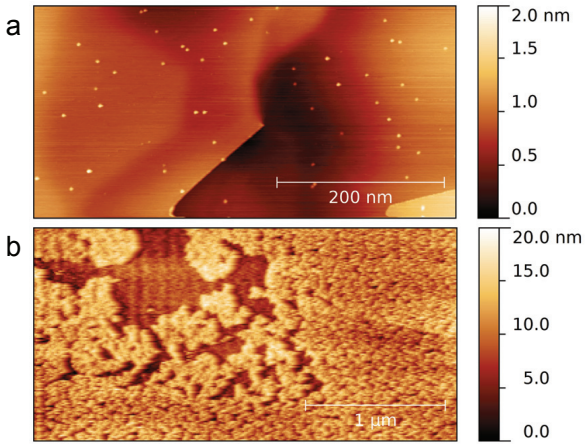

Figure 2.13.: Scanning tunneling microscopy (STM) images of deposited Cu clusters on highly oriented pyrolytic graphite (HOPG). (a) Cu_{100} clusters deposited with an impact energy of about 4 keV per cluster. Due to the high deposition energy the clusters create damages in the surface during landing and get pinned. (b) Cu_{2000} clusters deposited with an impact energy of about 1 keV per cluster. In this case the deposition energy is ≈ 0.5 eV/atom and falls within the soft landing regime. The clusters stay mobile on the surface and create large agglomerates.

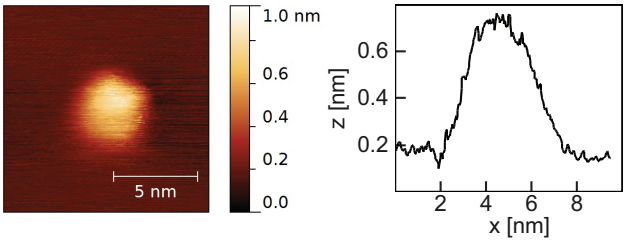

Figure 2.14.: High resolution scanning tunneling microscopy (STM) image of one of the Cu_{100} clusters from Fig. 2.13 and the corresponding horizontal cross-section.

2.8 Conclusions

In this chapter a new CIBD system was presented and its various components were described and explained in detail. The system was designed with a strong emphasis on cluster purity, deposition accuracy, and reproducibility. Two different deposition stages are incorporated in the system and available for cluster deposition and sample synthesis. The first stage was designed for the deposition of large amounts of clusters, utilizing the native mass distribution produced by the source, which can be monitored with a TOF and controlled via the source parameters. The second stage is optimized for the deposition of smaller amounts of precisely mass-selected clusters in combination with optional matrices under ultra clean conditions. The impact energies of the clusters can be varied within a wide energy range and, during deposition, the sample can be either cooled or heated. A special custom-designed combination of a sample holder and a mask together with the two deposition stages allows the production of homogeneous cluster/matrix samples with well-defined clusters amounts. The system was tested in first deposition experiments with Cu clusters.

3 Cluster/matrix nanocomposites: Iron/Silver and Iron/Chromium

Selected parts of this chapter have also been published in [14] and [20] within the framework of this thesis. The respective paragraphs – with minor conformations included – are indicated by a vertical gray bar at the inner page margin[1].

In this chapter experiments and data obtained on two different cluster/matrix combinations are presented: Fe/Ag and Fe/Cr. While the system Fe_x/Ag (Chap. 3.2) was mainly used to probe and to demonstrate the abilities of the CIBD system, the focus of the experiments on Fe_x/Cr (Chap. 3.3) was to thoroughly study the magnetic characteristics of the material system. Since size-selected clusters embedded in a matrix were needed for both experiments the second deposition stage (Chap. 2.4.2) was used for the sample preparation.

3.1 Motivation

Today's metallic alloys are prepared using complex thermo-mechanical treatment steps, that are, quenching, annealing combined with plastic deformation, in order to obtain the multicomponent multiphase structures that are optimized for advanced structural and functional applications. Besides the pathways for the synthesis of the alloys, their final nano- and microstructure is strongly determined by their phase diagrams. This limits the extent of possible deviations from the corresponding well-defined thermodynamic equilibrium, what determines the volume fraction of precipitates or second phase particles present in the alloy as well as the composition of the matrix phase. Oxide dispersion strengthened alloys are the exception, since the distribution of oxide particles in the metallic matrix can be modified without the above mentioned constraints, since the processing is done by mechanical alloying, not via the melt route followed by thermo-mechanical treatments as it is usually done as described above. On the other hand, in metallic multiphase alloys, the ranges of precipitate sizes and their distribution widths, as well

[1] *Reprinted with permission from* [14]. ©2015, AIP Publishing LLC.

as the chemical composition of the precipitates and that of the matrix, are severely limited by the thermodynamics of the alloy systems. Therefore, the potential for an ultimate alloy design will remain an elusive goal as long as a thermo-mechanical treatment is employed for processing the alloys.

The simultaneous deposition of preformed clusters, co-deposited with a molecular beam of another element (the matrix) on a substrate opens a way to overcome the above mentioned limitation. There is a rich literature regarding the synthesis of charged clusters of basically any element and of many alloy systems and their transfer into UHV systems. The deposition of the charged clusters onto substrates can be performed using variable impact energies. Such a process opens an effective, yet highly versatile, new route for the synthesis of cluster-based alloys, that is, multiphase alloys with very tight control of the fraction of clusters inside a matrix consisting of another element or of an alloy system.

In this chapter, the experiments and results obtained on two different cluster/matrix combinations are presented: Fe/Ag (Chap. 3.2) and Fe/Cr (Chap. 3.3). The first being rather simple, with only limited interactions between the matrix and the clusters, and the latter being more complex due to the magnetic interactions between the matrix and the clusters, that can highly affect the magnetic characteristics of the samples.

3.2 Iron clusters in a silver matrix

In this section, experiments, demonstrating the capabilities of the CIBD system on the basis of Fe clusters embedded in an Ag matrix, are presented and discussed. Among other findings, the experiments revealed, that the apparatus allows to produce cluster-based thin films with outstanding precision, in terms of cluster amount and sample homogeneity.

3.2.1 Introduction

As an illustrative example for a model system, of a cluster/matrix combination, yielding insight into the microscopic as well as the macroscopic characteristics of the samples, Fe clusters embedded within an Ag matrix, were chosen. The focus of these experiments was to test and evaluate the general capabilities of the apparatus, in terms of achievable sample homogeneity and the precision of the deposited cluster amounts, while at the same time, to gain information about the characteristics of individual clusters as well as their arrangement within the matrix.

The Fe clusters are superparamagnetic above their blocking temperature (T_B) and their magnetic properties are extremely sensitive to the cluster size, spatial distribution, and their interactions with the matrix. Therefore, measuring the magnetic properties of the clusters embedded in the matrix provided an elegant and effective way for their accurate characterization. In this particular case, Ag was chosen as a matrix for two reasons: first, different from the Fe clusters, Ag is diamagnetic and, secondly according to the Ag-Fe binary phase diagram [21], Ag and Fe are immiscible. Therefore, as little as possible magnetic and chemical interactions between the clusters and the matrix should occur. Consequently, only small modifications in the individual cluster characteristics were expected.

3.2.2 Experimental details

The superparamagnetism of Fe clusters was studied, using a superconducting quantum interference device (SQUID) magnetometer, where zero field cooled/field cooled (ZFC/FC) curves and isothermal magnetization loops were measured. The main magnetic characteristics such as superparamagnetic blocking temperature (T_B) and saturation magnetization (M_{sat}) were deduced from these magnetic data. A subsequent analysis of the magnetic characteristics yielded important insights into the cluster properties, for example, the value of T_B is a direct function of the cluster size, the value of M_{sat} can provide a measure for the amount of magnetic material (clusters) present in the samples, and the shape of the magnetization curve can be related to the cluster size or to their possible aggregation.

Fe_x/Ag samples with 2, 10, 50, and 100 vol.% Fe_{1000} were synthesized with a deposition energy of 50 eV/cluster. Since each of the samples nominally contains the same amount of Fe_{1000}, namely an equivalent Fe cluster film thickness of 6 nm, this resulted in Ag matrix thicknesses of roughly 294, 54, 6 and 0 nm, respectively.

To minimize cluster mobility during deposition, the sample holder was cooled with liquid nitrogen and kept cooled until the sample preparation was completed. For all the prepared samples, an Si wafer, with a native oxide layer and covered with a 2 nm Ta adhesion layer, was used as a substrate. In addition, prior to the deposition of the clusters and Ag matrix, the Ta layer was covered with 5 nm Ag buffer layer. And, after the deposition of the cluster film, a 20 nm Ag capping layer was added. The buffer layer ensured that the clusters are only in contact with Ag, while the capping layer protected the samples against oxidation after sample preparation and during subsequent measurements, for example, with the SQUID.

3.2.3 Results and discussion

EDX characterization

The elemental composition of each of the samples was verified by energy dispersive X-ray spectroscopy measurements (EDX) (Tab. 3.1). For all the samples, the EDX measurements showed, that the sample composition as well as the Fe cluster film thickness (computed from the corresponding volume fraction), differed only by roughly 10 % from the target values, for all samples. Furthermore, in order to obtain a measure of the spatial distribution of the clusters, for one of the samples a 2D array of 225 EDX spectra over the entire sample surface were measured. Figure 3.1 shows the resulting map of the Fe concentration. As usual, during cluster and matrix deposition, the substrate was covered with one of the specifically designed masks (Fig. 2.7) to ensure for precise sample synthesis. For this particular sample, the mask had a diameter of 2 mm and its approximate position, which delimits the area that was not covered by the mask and is indicated by the red circle in figure 3.1. A statistical evaluation of the EDX spectra, taken at the sample area, yielded a deviation of the Fe concentration from its mean value by less than 10 %. Both results, that is the overall sample composition as well as the achieved homogeneity, clearly demonstrate the unique capabilities of the system in general, and, in particular, the advantages of the developed deposition stage and the specially designed sample holders. To date, to our knowledge, similar results have not been reported in the literature on other CIBD systems.

Table 3.1.: Energy-dispersive X-ray spectroscopy (EDX) measurements of the sample composition and Fe cluster film thicknesses for the various Fe_{1000}/Ag samples.

vol.% Fe_{1000}		Fe_{1000} thickness [nm]	
Nominal	EDX	Nominal	EDX
2	1.8(2)	6	5.5(5)
10	9(1)	6	5.3(5)
50	48(5)	6	5.5(5)
100		6	6.4(6)

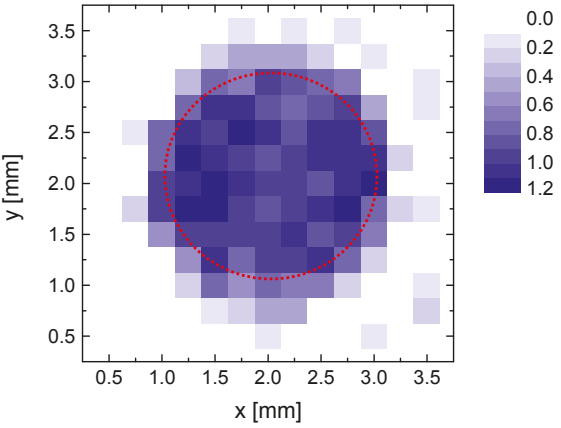

Figure 3.1.: Map of the normalized Fe concentration in a typical Fe_x/Ag sample recorded by Energy-dispersive X-ray spectroscopy (EDX). The nominal Fe concentration was normalized to 1. The red circle indicates the part of the substrate that was not covered by the mask (diameter 2 mm) and where clusters were deposited. Pixels close to the edge of the mask may feature wrong amounts, since they were just partly covered.

Magnetic properties

Standard ZFC/FC measurements on the samples were conducted with an applied magnetic field of $\mu_0 H = 20\,\mathrm{mT}$ (Fig. 3.2). The magnetic measurements were performed on the samples in the in-plane geometry, meaning that the magnetic field was applied parallel to the sample surface; this measurement geometry was used for all magnetic data included in this thesis. For the 2 vol.% Fe sample, T_B is below 10 K and, subtracting a background arising from the Si substrate, the ZFC/FC curve shows a 1/T dependence for temperatures above T_B. This is indicative of well-separated clusters, with hardly any magnetic interactions. By contrast, the 10 vol.% Fe and 50 vol.% Fe samples exhibit a T_B of 35 K and roughly 120 K respectively, suggesting increasing magnetic interactions and the formation of aggregates, especially for the 50 vol.% Fe sample. For the 100 vol.% Fe (only Fe clusters) sample, the ZFC/FC curve shows only little variation of the magnetization with temperature. This implies that this sample displays a magnetic behavior, that is virtually the same as that of an Fe thin film.

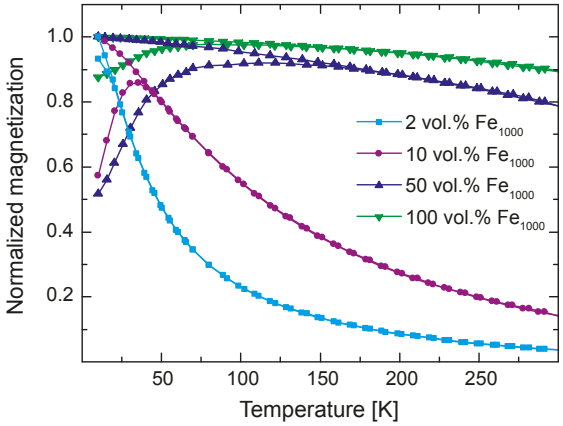

Figure 3.2.: Zero field cooled/field cooled (ZFC/FC) curves of Fe_{1000} cluster/Ag matrix samples with 2, 10, 50 and 100 vol.% Fe. The ZFC/FC curves were measured with a superconducting quantum interference device (SQUID) magnetometer with an applied magnetic field of $\mu_0 H = 20$ mT.

In order to obtain information about the size of the clusters and to look for indication of their possible aggregation and magnetic interactions, magnetization loops were measured at 300 K and then fitted with Langevin functions (Fig. 3.3). Assuming bulk Fe magnetic moment of 2.2 Bohr magneton (μ_B) per atom, the fit to the magnetization loop of the 2 vol.% Fe sample yielded a cluster size slightly above 1000 atoms, perfectly corroborating the number selected by the mass separation. For the 10 vol.% Fe_{1000} and 50 vol.% Fe_{1000} samples larger average cluster sizes of the order of 2000 and 18000 atoms were determined. This is an indication of cluster aggregation or at least of strong magnetic interactions of the clusters occurring in the 10 vol.% Fe_{1000} and 50 vol.% Fe_{1000} samples. While the fit to the magnetization loop of the 2 vol.% Fe_{1000} sample almost perfectly matches the data, small discrepancies are present for the 10 vol.% Fe_{1000} sample, but especially for the 50 vol.% Fe_{1000} sample. This indicates that, due to the high degree of agglomeration or magnetic interaction of the clusters, fitting the data, by assuming a single cluster size, is not a valid assumption. In these cases, it would be necessary to assume a broad distribution of agglomerated clusters in order to achieve better fit to the data.

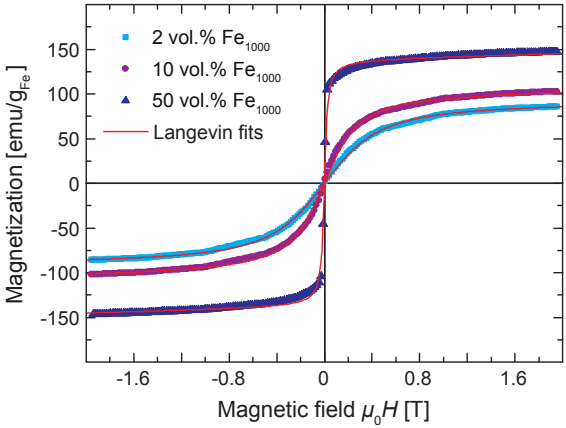

Figure 3.3.: Magnetization loops of the Fe_{1000}/Ag samples with 2, 10 and 50 vol.% Fe_{1000} recorded at 300 K. The data were fitted with Langevin functions. The fits revealed pronounced agglomeration of the clusters in the 10 vol.% Fe_{1000} sample, and especially in the 50 vol.% Fe_{1000} sample, while no agglomeration occurs in the 2 vol.% Fe_{1000} sample.

After field-cooling the samples with an applied magnetic field of $\mu_0 H = 4.5\,\mathrm{T}$ magnetization loops for the series of samples were also measured at 5 K (Fig. 3.4). For comparison purpose, especially for the 100 vol.% Fe_{1000} sample, a 6 nm Fe thin film was also deposited via MBE. Except for the different deposition technique, the sample structure was exactly the same as for the Fe cluster samples. After subtracting a linear background, arising mainly from the diamagnetic Si substrate, M_{sat} was determined for all samples. The lowest value of M_{sat} was found for the 2 vol.% Fe_{1000} sample ($\approx$110 emu/g_{Fe}), the value of M_{sat} increases with the cluster concentration, reaching its maximum of $\approx$190 emu/g_{Fe} for the 100 vol.% Fe_{1000} cluster film. The value of M_{sat} for the MBE deposited Fe thin film is roughly the same as that of the 100 vol.% Fe_{1000} cluster film. This value is slightly less than the 220 emu/g_{Fe} one would expect for bulk Fe.

For all cluster samples it was found that the magnetization loops measured at 5 K after field cooling the samples in a magnetic field of 4.5 T, are horizontally shifted (not shown). In general, this shift, known as an exchange bias, resulting from the coupling of a ferromagnet with an antiferromagnet or ferrimagnet at the interface [22]. Since Fe and Ag are the only elements that were present in the samples

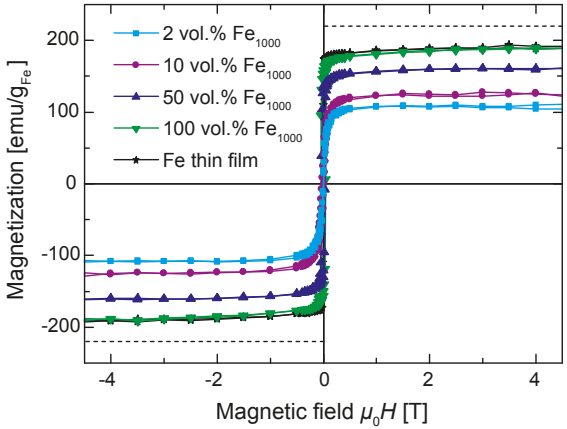

Figure 3.4.: Magnetization loops of Fe_{1000}/Ag samples with 2, 10, 50 and 100 vol.% Fe_{1000} and for comparison an Fe thin film with the same nominal Fe thickness as that of the cluster films. Black dotted lines: bulk Fe magnetic moment 220 emu/g_{Fe}. The measurements were conducted at 5 K after field cooling the samples from 300 K in a magnetic field of 4.5 T. All data were corrected for linear (para- or diamagnetic) background.

and neither is an antiferromagnet or a ferrimagnet, oxidation of the samples during the deposition and formation of ferrimagnetic Fe_2O_3 or of Fe_3O_4 [23] must be considered. The measured exchange bias, being between 0.9 mT for the 2 vol.% Fe_{1000} sample and 3.4 mT for the 100 vol.% Fe_{1000} sample is rather small for the Fe/Fe_xO_y system. This suggests that only a small fraction of the Fe is oxidized [23]. This assumption is corroborated by the high M_{sat} of the 100 vol.% Fe_{1000} sample, which would be drastically reduced if larger fractions of Fe_2O_3 or Fe_3O_4 would have been formed ($M_{sat} = 114$ emu/g_{Fe} and 131 emu/g_{Fe}, respectively).

Discussion

The results obtained from the magnetic characterization of the Fe_{1000}/Ag samples, in particular the ZFC/FC measurements and the Langevin fits to the magnetic hysteresis loops recorded at 300 K, show, that the samples with 2, 10 and 50 vol.% Fe_{1000} can be divided into two groups. While for the 2 vol.% Fe_{1000} sample the clusters are neither agglomerated, nor magnetically interacting, for the 10 and

50 vol.% Fe_{1000} samples agglomeration and/or magnetic interaction occur. Therefore, in the following, starting with the 2 vol.% Fe_{1000} sample, the samples will be discussed separately.

The results from the magnetic characterization and the EDX analysis of the 2 vol.% Fe_{1000} sample yielded the following. First, it was found (for all samples), that the measured M_{sat} is not matching the value, that would be expected for the respective amount of Fe in the sample (220 emu/g). For the 2 vol.% Fe_{1000} sample this discrepancy is about 50 % of the nominal value. Secondly, the EDX analysis of the sample revealed (for all samples), that the total amount of Fe (atoms) being present in the sample matches the amount of Fe, that was supposed to be deposited in the form of clusters and that was measured at the sample during preparation by counting impinging clusters (according to the procedure described in chapter 2.4). Thirdly, the Langevin fit to the magnetization loop of the 2 vol.% Fe_{1000} sample recorded at 300 K showed, that the magnetic moment per particle in the sample is 2200 μ_B. Assuming a magnetic moment of 2.2 μ_B per Fe atom (value of bulk α-Fe) this means, that all clusters being present in the sample consist of 1000 atoms, as selected by the mass-separation unit.

Considering these findings several explanations are possible for the reduction of the total M_{sat} in the 2 vol.% Fe_{1000} sample:

a. The magnetic moment of the individual Fe atoms is reduced by 50% down to 1.1 μ_B per atom and all clusters in the sample have 2000 atoms (would match the 2200 μ_B/particle). This is in principle possible, but rather unlikely. First because of the necessary drastic reduction of the magnetic moment per Fe atom by 50 % and secondly it would mean, that always exactly two of the deposited Fe_{1000} clusters in the sample are agglomerated or strongly magnetically interacting.

b. 50% of the clusters are, due to constraints of the Ag matrix, in a non-magnetic phase (e.g. face-centered cubic, fcc), while the other 50 % of the clusters still consist of 1000 atoms/cluster with a magnetic moment of 2.2 μ_B per Fe atom. However, results obtained from a recent, preliminary transmission electron microscopy (TEM) study (being not part of this thesis) did not show any hint for fcc Fe in the 2 vol.% Fe_{1000} sample.

c. Other explanations as partial dissolving of the outer shells of the clusters (with the dissolved Fe atoms being not ferromagnetic) can be discarded, since that is not consistent with the results obtained from the Langevin fit to the data.

d. 50% of the clusters were completely dissolved in the Ag matrix, while the remaining 50% of the clusters still consist of 1000 atoms with a magnetic moment of 2.2 μ_B per Fe atom. A speculative explanation might be the following; the first Fe clusters are deposited on an initially pure Ag surface. Due to their small diameters (2.8 nm) the clusters have high vapor pressures and consequently a potentially high solubility in the Ag matrix. Therefore the clusters might be completely dissolved. Subsequent clusters either land on an area being freshly covered with Ag (and are also dissolved), or they land on an area where the Ag is already saturated with Fe, can therefore not be dissolved, and survive the sample preparation. Higher Fe cluster vol % (less fresh Ag surface) might result in less clusters being dissolved in the matrix and consequently in higher values of M_{sat} of the samples, as observed for the 10 and 50 vol.% Fe_{1000} samples, respectively (Fig. 3.4).

As previously stated, in contrast to the 2 vol.% Fe_{1000} sample, the magnetic characterization of the 10 and 50 vol.% Fe_{1000} samples revealed agglomeration and/or magnetic interactions of the Fe clusters in these samples. The Langevin fits to the 300 K magnetization loops (Fig. 3.3) yielded magnetic particle sizes of 2000 and 18000 atoms. In both cases the fits are not perfectly matching the data when assuming a single cluster size. This indicates a broad size distribution of the magnetic particles in the matrix (in particular for the 50 vol.% Fe_{1000} sample). Both findings underline the mentioned aggregation of the clusters or magnetic cluster–cluster interactions in the 10 and 50 vol.% Fe_{1000} samples. The fact, that agglomeration and/or magnetic interactions only occur in the 10 and 50 vol.% Fe_{1000} samples and not in the 2 vol.% Fe_{1000} sample might be explained by the different average distances between neighboring clusters in the three samples. To approximate this distance for the actually randomly distributed clusters, a body centered cubic (bcc) arrangement of the clusters within the Ag matrix might be assumed. The corresponding center to center distance for neighboring clusters are 9.1 nm, 5.3 nm, and 3.1 nm in the 2, 10 and 50 vol.% Fe_{1000} samples, respectively. Since the nominal cluster size is 2.8 nm in all samples this means, that neighboring clusters are almost touching each other in the 50 vol.% Fe_{1000} sample, while in the 10 vol.% Fe_{1000} sample in average still less than one cluster diameter separates neighboring clusters. Furthermore, since these are only average values, many clusters are actually much less separated than the approximated center to center distances suggest. In contrast, in the 2 vol.% Fe_{1000} the approximated center to center distance is considerably higher and obviously sufficient to prevent the clusters from agglomeration and magnetic interaction.

3.2.4 Conclusions

In this section the capabilities of the CIBD system were demonstrated using Fe_{1000}/Ag samples containing different vol.% of Fe_{1000} clusters. It was shown that the apparatus permits to synthesize cluster-based samples with precisely predetermined cluster amounts (±10%), which are evenly distributed over the sample area (±10%). These capabilities underscore the degree of control that is achievable with the new apparatus. Such a degree of control in CIBD has not been previously reported in the literature. The magnetic data corroborated, that the co-deposition of clusters and matrix in combination with liquid nitrogen cooling of the sample during deposition, allow to synthesize samples with nearly no aggregation of the clusters for the case of small cluster volume fractions.

Although the pressure in the second deposition stage was in the 10^{-9} mbar range during source operation (Chap. 2), which is lower than that reachable in most CIBD setups, reported in the literature or commercially available, a detailed analysis of the cluster magnetic characteristics showed that the clusters get slightly oxidized during the long deposition times. In order to further reduce the level of oxidation, the purity of the deposition process will be drastically improved in the near future by the installation of an additional 2000 l/s cryo-pump in front of the second deposition stage.

Within the scope of the experiments being part of this thesis it was not possible to find a definite explanation for the observation that a fraction of the clusters within the Ag matrix seems to be not ferromagnetic. Further experiments comprising, amongst others, atom probe tomography and TEM might provide an explanation for the magnetically missing clusters.

3.3 Iron clusters in a chromium matrix

In this section, experiments carried out for exploring the magnetic characteristics of Fe clusters embedded in Cr matrix and the experimental data are presented and discussed. Since the ferromagnetic (FM) Fe clusters are magnetically interacting with the antiferromagnetic (AFM) Cr matrix via exchange interactions, in addition to the interaction among each other as discussed for the case of the Fe_x/Ag system, the Fe_x/Cr material system is more complex than the Fe_x/Ag material system presented in section 3.2. The magnetic characteristics of the samples were expected to be strongly depending on the cluster size as well the cluster density in the matrix, thus the second deposition stage (presented in Chap. 2.4.2) was used for sample synthesis.

3.3.1 Introduction

For the Fe_x/Ag nanocomposite it was shown that a full control over the sizes of the clusters and their distribution and volume fraction in the matrix can be achieved [14](Chap. 3.2). One of the objectives of the experiments with the Fe_x/Ag material system was to study the characteristics of the embedded Fe clusters in a matrix. Since Ag is diamagnetic, only weak magnetic interaction between matrix and the FM clusters were expected to take place. It was possible to gain information about, for example the size of the embedded clusters via magnetic measurements (Chap. 3.2.2). The intention of the work presented in this section was to progress one step further to a more complex cluster/matrix system by exchanging the magnetically passive Ag matrix with the magnetically active Cr. In fact, the AFM Cr was expected to possibly lead to potentially new and interesting effects, especially at the Fe cluster/Cr matrix interfaces. This is because at the interface between the FM and the AFM material a spin exchange coupling occurs and a part of the FM magnetic moments become pinned by the AFM Cr, resulting in an increased magnetic anisotropy manifesting itself as an exchange bias effect (EB) [24]. The EB effect gives rise to a horizontal shift of the magnetization loops, the EB field H_{EB}, and is usually accompanied by an increase of coercivity (H_C) and of T_B. The EB effect was first described by Meiklejohn and Bean in 1956 [25]. They investigated clusters with a FM Co core and AFM CoO shell and, consequently, they observed the characteristic horizontal shift of the hysteresis loops measured after field cooling the samples from temperatures above the Néel temperature (T_N) of CoO down to 77 K.

Since its discovery, the EB effect has been observed in numerous FM/AFM combinations such as core/shell clusters [26, 27], thin film systems [28, 29], and also

cluster/matrix combinations [30–32]. So far, most of the research has been focused on thin film systems due to their commercial importance for read heads in magnetic data storage [33]. Since many difficulties arise in fabricating FM cluster/AFM matrix systems, in a strictly controlled way, much fewer studies have been carried out on these latter systems, compared to those performed on thin films. In principle, there are two main approaches for the fabrication of FM cluster/AFM matrix systems. The first is to co-evaporate several materials or to chemically produce a compound in a first step and then to induce the formation of FM precipitates within the leftover AFM matrix in a second step (e.g. by heating) [34, 35]. The main drawback of this synthesis route is the lack of a close control over the size and density of the precipitates within the matrix. An alternative, effective approach is to co-deposit preformed FM clusters (e.g. by inert gas-condensation) and AFM matrix by physical vapor deposition, that is, atomic beams [30–32]. Using this combination of cluster and atom beam deposition, the cluster size can be well-defined and, by closely controlling the exact deposition rates of both, the clusters and the matrix, the amount of clusters in the matrix can also be exactly selected. However, to date, only a few studies on the EB effect in cluster/matrix nanocomposites have been published and, of the published few, most were based on a very limited number of samples.

In this section, a comprehensive study of the magnetic characteristics in the system of preformed Fe clusters embedded in Cr a matrix are presented. It is based on the largest series of samples (20) for any FM/AFM cluster/matrix combination previously reported in literature. Due to the large amount of samples, representing three different cluster sizes and a broad range of cluster concentrations in the matrix, combined with a high degree of control over the experimental conditions, the effects of the two critical parameters, cluster size and density within the matrix on T_B, H_C and H_{EB} could be clearly shown. The system Fe_x/Cr is a perfect model system: being just based on two elemental components, it avoids the pitfall of compositional variations in the AFM (e.g. the case of only partially oxidized CoO) which may lead to additional, complicating effects. Furthermore, according to their binary phase diagram Fe and Cr are immiscible for most compositions [36, 37], which helps to maintain the desired cluster/matrix structure.

3.3.2 Experimental details

Since both, thorough mass selection as well as a matrix were needed for the experiments, the samples were prepared using the second deposition stage (Chap. 2.4.2). To minimize the deformation of the clusters during deposition, they were decelerated to 50 eV, prior to deposition and then soft-landed on an Si substrate with a native oxide layer (conducting). In order to minimize migration and agglomeration of the clusters, the substrate was cooled with liquid nitrogen throughout the sample synthesis. The Cr matrix was co-deposited using the effusion cell. The pressure in the deposition chamber was maintained in the 10^{-9} mbar range during deposition.

The complete Fe_x/Cr samples consist of the Si substrate with a native oxide layer, a 10 nm Cr base layer, the Fe cluster/Cr matrix layer, a 10 nm Cr top layer and a 10 nm Au film for oxidation protection. This geometry makes sure that the Fe clusters are in contact with Cr only and no oxidation of the clusters takes place after the deposition. To allow for a detailed comparative study of the magnetic characteristics of the samples, a 6 nm equivalent thickness of clusters was deposited on all samples and the Fe cluster concentration was adjusted by the amount of deposited Cr. Fe_x/Cr samples were produced with Fe cluster sizes of 500, 1000 and 2000 atoms per cluster, corresponding to cluster diameters of 2.3, 2.8 and 3.6 nm, respectively, and cluster volume fractions ranging from 2 vol.% to 50 vol.%.

3.3.3 Results and discussion

Reproducibility tests

First trial experiments with Fe_{1000}/Cr samples yielded a totally erratic behavior of their magnetic characteristics. Additional tests revealed that, without active temperature stabilization of the second deposition stage, the temperature of the whole stage varied measurable from sample to sample (up to 50 K). These variations in stage temperature might be due to different temperatures of the effusion cell during sample preparation (necessary to obtain different evaporation rates), resulting in different amounts of heat being transferred to the stage via thermal radiation. Therefore, variations in temperature of the sample surface (which is directly facing the evaporator) might be even larger than the measured 50 K at the stage itself. After further testing, it was concluded that, cooling the deposition stage during deposition with liquid nitrogen as well as gluing the sample to the sample holder with silver glue (for a better heat transfer), while maintaining similar deposition times

(and rates) for the individual samples, it was possible to obtain reproducible sample characteristics. Regarding the cooling requirement, any kind of temperature stabilization might be sufficient, but cooling to the lowest possible temperature is anyway beneficial for cluster-based samples, since it suppresses movement of the deposited clusters and, consequently, also their aggregation.

In order to finally prove the reproducibility of the sample characteristics, three identical Fe_{1000}/Cr samples with 10 vol.% Fe_{1000} were prepared as previously described and magnetically characterized with a SQUID magnetometer. For the magnetic characterization, ZFC/FC magnetization curves and magnetic hysteresis loops were recorded. The results are shown in figures 3.5 and 3.6.

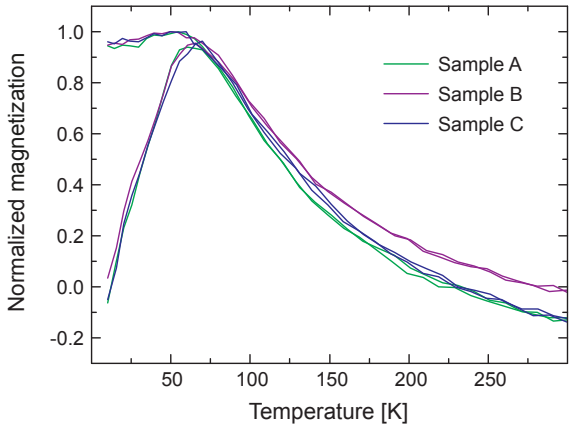

Figure 3.5.: Zero field cooled/field cooled (ZFC/FC) magnetization measurements of three identical Fe_{1000}/Cr samples with 10 vol.% Fe_{1000} prepared for reproducibility tests. The resulting blocking temperatures (T_B) as well as the overall shapes of the ZFC/FC curves are nearly identical for the three samples.

From the magnetization data, it is clearly visible that the three samples are magnetically almost identical. The ZFC/FC curves as well as the magnetization loops have basically the same shape and thus it is hard to distinguish between the three samples. In fact, according to experience, the slight variations in the magnetic response, observed from sample to sample, are of the order of the variations that are typically observed from repeated sets of measurements carried out on a single sample, caused by slight differences in sample mounting.

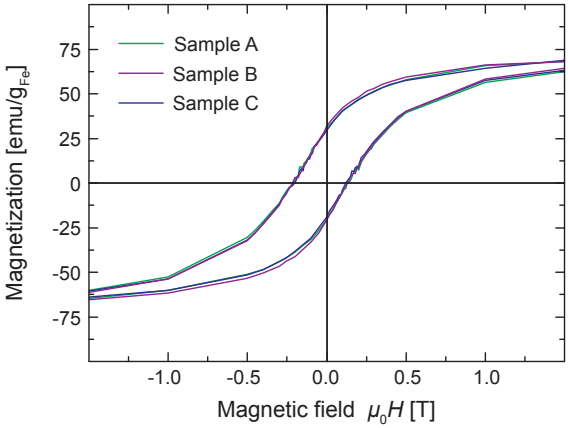

Figure 3.6.: Magnetization loops of three identical Fe_{1000}/Cr samples with 10 vol.% Fe_{1000} measured at 5 K. The shape of the three magnetization loops is basically identical.

Accordingly, the series of samples described in section 3.3.2, was prepared as previously described, using similar deposition times, cooling of the deposition stage with liquid nitrogen throughout the sample synthesis, and having the Si substrates glued to the sample holder.

TEM characterization

Figure 3.7 shows energy filtered transmission electron microscopy (EFTEM) and scanning transmission electron microscopy (STEM) micrographs of the Fe distribution for a 10 vol.% Fe_{1000}/Cr sample that was specifically prepared for TEM examination. To avoid the focused ion beam (FIB) cutting, typically used for the preparation of thin film samples for TEM examination, and possible oxidation of the prepared sample, the sample was directly deposited on a TEM grid covered with a thin amorphous C film. The overall sample thickness, including top and bottom Cr, layers was just 5 nm, being thin enough for TEM examination without further processing. Deposition parameters such as the cluster deposition rate and the sample temperature during deposition were identical to those used for the other samples. The EFTEM micrograph clearly shows that the Fe clusters are evenly distributed within the Cr matrix and no significant agglomeration had occurred. In

the STEM image, individual Fe clusters are clearly visible. Their size can be estimated to be roughly 3 nm which matches quite well the expected value of 2.8 nm. Additional diffraction data from TEM (not shown here) revealed that, as expected, the Fe clusters as well as the Cr matrix both retain the bcc structure.

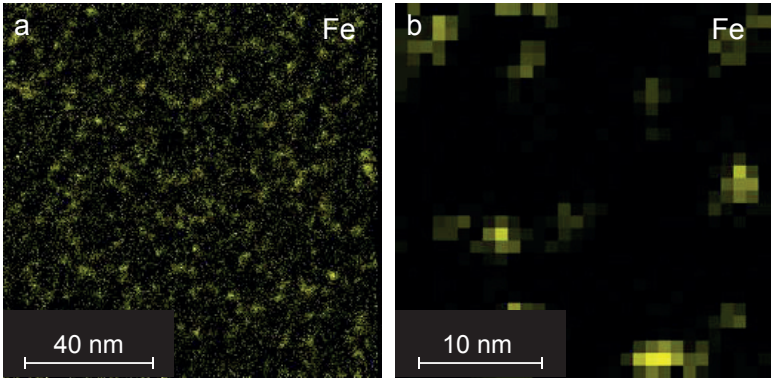

Figure 3.7.: (a) Energy filtered transmission electron microscopy (EFTEM) and (b) scanning transmission electron microscopy (STEM) micrographs of a 10 vol.% Fe_{1000}/Cr sample prepared on a transmission electron microscopy (TEM) grid + amorphous carbon film with an Fe cluster equivalent thickness of 0.2 nm. The EFTEM image shows the Fe cluster distribution in the sample and the STEM image shows individual Fe clusters. The STEM image was recorded using energy-dispersive x-ray spectroscopy (EDX) and the Fe K signal.

Magnetic properties

In the following paragraphs the magnetic properties of the Fe cluster assemblies in the Cr matrix are discussed. The magnetic characteristics are determined from standard ZFC/FC magnetization curves and magnetic hysteresis loops measured with a SQUID magnetometer.

The ZFC/FC curves were measured with an applied magnetic field of $\mu_0 H = 20\,\mathrm{mT}$ in the temperature range between 10 K and 350 K. As previously described, the measurements were conducted in the in-plane geometry.

Figure 3.8 shows the T_B for the Fe_x/Cr samples determined from the ZFC/FC curves. At this point it is reasonable to assume, that the natural parameter influencing possible interactions between the clusters, is rather the average distance

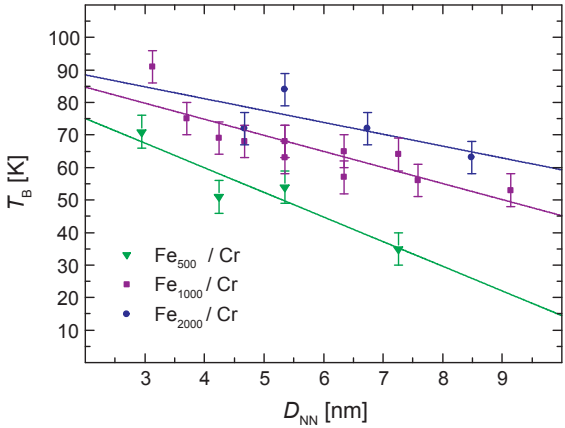

Figure 3.8.: Blocking temperature (T_B) versus nearest neighbor distance (D_{NN}) for Fe_x/Cr samples. The solid lines on the three series of samples with 500, 1000 and 2000 atoms are just guides to the eye. A clear dependence of T_B on the cluster size as well as D_{NN} is evident.

among neighboring clusters than the cluster vol.% in the matrix. To approximate this distance, for the actually randomly distributed clusters, a bcc arrangement of the clusters within the matrix was assumed and the T_B (and subsequent magnetic data) were plotted versus the, under this assumption, estimated nearest neighbor distance D_{NN}. The data plotted in this way reveal that T_B is indeed affected by both the size of the embedded Fe clusters as well as the D_{NN}. The T_B are higher for larger clusters and they rise nearly linearly (within the investigated region) with decreasing D_{NN}, with the linear slope being smaller for larger clusters. Thus, the differences in the T_B values among the three cluster sizes become distinctly smaller for smaller D_{NN} (i.e. for higher cluster vol.%). To minimize the influence of cluster–cluster interactions, their dependency on the cluster size should be first considered for the larger cluster distances. As a starting point for analyzing the data, one could first consider the simplest model of non-interacting particles with an uniaxial anisotropy within a non-magnetic matrix. In such a case, one would expect a simple proportionality relation of the form $T_B \propto K_{eff}V$, where K_{eff} is the effective anisotropy constant and V is the particle volume. Indeed, the measured T_B values show some rudimentary size dependence, especially for large D_{NN}, but they do not scale linearly with the cluster size. Also, the estimated K_{eff} of 0.8 to

$1.3 \times 10^6\,\mathrm{J/m^3}$ is almost two orders of magnitude larger than the value one would expect for clusters with the magnetocrystalline anisotropy of bulk α-Fe. Both of the above results lead to the conclusion that for clusters, in the highest state of dilution, the effective anisotropy constant is determined by magnetic exchange interactions with the Cr matrix. This assertion is further corroborated by a direct comparison with the assembly of Fe clusters embedded in a nonmagnetic Ag matrix (Sec. 3.2). The Fe_{1000} clusters with $D_{NN} \approx 9$ nm (2 vol.% Fe_{1000}) were studied earlier and their T_B was about 6 K [14]. An increase of the T_B by almost one order of magnitude to 53 K, for the Fe_{1000} clusters deposited in the AFM Cr matrix unambiguously points out the decisive role played by the FM/AFM exchange coupling in significantly enhancing the magnetic anisotropy. For lower D_{NN}, the effect of the particle size on T_B gets even less pronounced, since magnetic inter-particle interactions (e.g. strong dipole-dipole interactions) become dominant.

Magnetic hysteresis loops were measured at 5 K, after field cooling the samples from 350 K, being above the T_N of Cr (311 K [38]), in an applied magnetic field of $\mu_0 H = 4.5$ T. A linear diamagnetic background, originating from the Si substrate as well as the Au layers was subtracted from the magnetic data. The coercive field H_C of the samples can be derived from the measured hysteresis loops as $H_C = \left(H_C^+ - H_C^-\right)/2$, with H_C^+ and H_C^- being the external magnetic field values for which the magnetization $M = 0$ at the positive and negative branches of the magnetic hysteresis loops, respectively. The obtained H_C for the three sample series are shown in figure 3.9.

In the investigated region, H_C displays no clear dependence on the size of the embedded Fe clusters, but it increases slightly with decreasing D_{NN} from roughly 1550 Oe (for $D_{NN} \approx 9$ nm) to around 2000 Oe (for $D_{NN} \approx 3$ nm). This behavior shows that H_C mainly depends on the local anisotropy of the Fe clusters and it rather weakly rises for smaller D_{NN} due to extra anisotropy coming from interactions between the individual Fe clusters. Comparing again the Fe_{1000}/Cr sample with $D_{NN} \approx 9$ nm (2 vol.% Fe_{1000}) with the aforementioned Fe_{1000}/Ag sample with the same cluster vol.% a significant rise in H_C from 56 Oe for Fe_{1000}/Ag to 1543 Oe for Fe_{1000}/Cr is found, underlining again the distinct rise in the anisotropy constant K_{eff} due to the FM/AFM interactions of the Fe clusters with the Cr matrix.

The horizontal shift of a magnetic hysteresis loops is described by $H_{EB} = \left(H_C^+ + H_C^-\right)/2$. Figure 3.10 shows the H_{EB} extracted from the magnetic hysteresis loops of the different samples. The EB values are basically independent of D_{NN}. The largest series of the Fe_{1000}/Cr samples obeys a linear behavior with a negligible slope of 2.4(4.5) nm $\mathrm{Oe^{-1}}$. Therefore, the data can be described within the error with a horizontal line, implying that the Fe cluster vol.% have either no or only little influence on H_{EB}. On the other hand, comparing the average H_{EB} values of

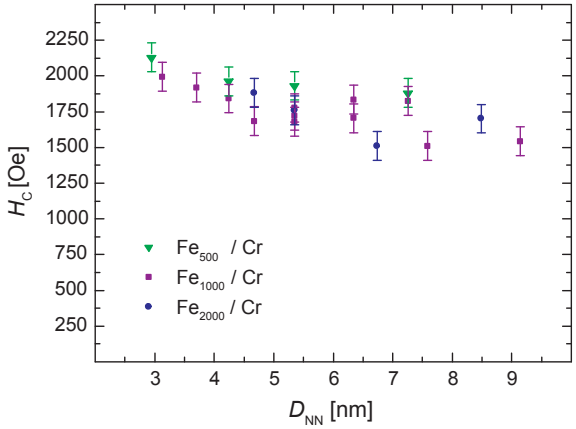

Figure 3.9.: Coercive field (H_C) versus nearest neighbor distance (D_{NN}) for Fe_x/Cr samples. H_C mainly depends on D_{NN}, no clear effect of the cluster size is evident in the investigated region.

the three series with different cluster sizes, the cluster size has a pronounced effect on the H_{EB}, as it is clearly visible in figure 3.10 b. Fitting horizontal lines to each series, one obtains average values of H_{EB} of 559(16) Oe, 442(7) Oe and 338(10) Oe respectively for the Fe_{500}/Cr, Fe_{1000}/Cr and Fe_{2000}/Cr sample series.

To model the dependence of H_{EB} on the cluster size, one should keep in mind that in first approximation the EB effect is an interface phenomenon. When the FM Fe clusters are cooled, in the presence of a magnetic field, down below T_N of the Cr matrix, the FM Fe clusters lock the AFM Cr domains in a certain direction via FM/AFM exchange interactions. The initial orientation of the AFM domains determines the unidirectional anisotropy axis, which is manifested by a shift of the magnetization hysteresis loops. For spherical FM clusters, one can assume that FM spins residing on the surface of the clusters are exchange coupled to their AFM neighbors, with a strength, that is determined by the exchange integral J. The FM/AFM interaction keeps all the spins of the cluster along the unidirectional anisotropy axis. During the magnetization switching process the external magnetic field flips the magnetization in the opposite direction. The switching field must overcome the FM/AFM coupling which is proportional to J times the cluster surface area πR^2, where R is the cluster radius. On the other hand, the bigger the magnetization of the cluster ($\propto R^3$ i.e. volume) the easier is rotating it away from

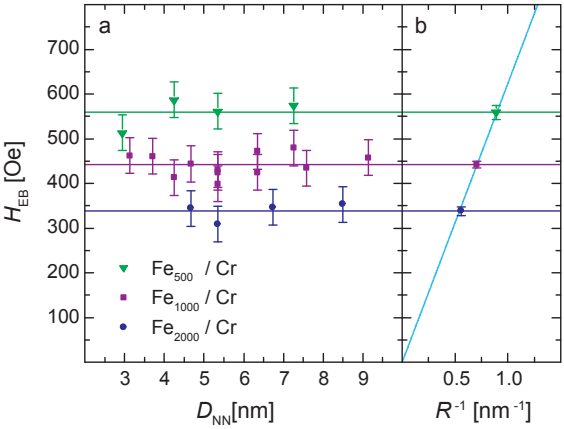

Figure 3.10.: (a) Exchange bias field (H_{EB}) versus nearest neighbor distance (D_{NN}) for the three series of samples with different cluster sizes. D_{NN} has no effect on H_{EB}, while a pronounced effect is found for the size of the embedded clusters. (b) Average H_{EB} versus the inverse particle radius (R^{-1}) for the three cluster sizes showing a linear relation.

an easy axis. Therefore, the switching field is proportional to the ratio JR^2/R^3 which eventually results in $H_{EB} \propto 1/R$. Plotting the obtained H_{EB} values for the three cluster sizes versus $1/R$ of the clusters (Fig. 3.10 b) and assuming $H_{EB} = 0$ for an infinitely large particle ($1/R = 0$), a linear relation is found and a linear fit to the data yields a slope of 624(7) $\mathrm{Oe^{-1}nm^{-1}}$. This straightforward relation, between H_{EB} and R of the embedded clusters, has never been clearly shown and reported for any FM/AFM cluster/matrix system.

As a way of comparison, one can look at the closely related core/shell nanoparticles featuring a FM core and an AFM shell. In that case, a theoretical study predicted an oscillatory relationship between H_{EB} and R [39]. For further comparison, one can also refer to the case of thin film systems consisting of a FM and an AFM layer. Restrepo-Parra et. al. [40] showed that $H_{EB} \propto 1/D^{m}$, with m ≈ 1 and D being the thickness of the FM layer. These previous results nicely support the present finding, since in both studies it is clear that H_{EB} is basically proportional to the surface to volume or interface to volume ratios of the FM portion of the material system.

The Fe_x/Cr system was already studied and previously reported in a publication by Qureshi et al. [32]. Their study is based on three samples with different cluster volume fractions, composed of clusters of a single size (≈340 atoms/cluster). Amongst their findings these authors reported that H_C and H_{EB} were both found to increase with increasing cluster vol.%. Compared to the results shown in this thesis, the behavior of H_C exhibits a similar trend with the absolute values being three to five times lower. For H_{EB} the values are between two and five times lower than the lowest H_{EB} value observed in this thesis (310 Oe). In addition, Qureshi et al. in their study showed a dependence on the cluster vol.% that is consistent with the findings of the present study. Of course these discrepancies cannot be easily accounted for. However, it is worth repeating here that, as discussed in section 3.3.3, it was found that a high degree of control over the deposition parameters is of utmost importance for consistently obtaining reliable and repeatable data. Possibly, a lack of close control of the the deposition parameters in the study of Qureshi et al. [32], could be at the base of some of the discrepancies between theirs and the present study's results.

3.3.4 Conclusions

In conclusion, using the UHV CIBD system a series of samples with Fe clusters embedded in a Cr matrix was obtained in a highly reproducible way. Subsequently, the magnetic characteristics of 20 samples with three different cluster sizes and varied cluster volume fractions were studied to determine their relevant magnetic parameters: T_B, H_C and H_{EB}. While T_B is found to be dependent on the size of the embedded clusters as well as on the average distance between neighboring clusters, D_{NN}, H_C is found to be rather weakly dependent on D_{NN}. The exchange bias field, H_{EB}, responds to the size of the embedded clusters according to the relationship, $H_{EB} \propto 1/R$ but it is not dependent on the cluster concentration in the matrix. With this observation one can draw the conclusion that the exchange bias effect is a rather local effect and it is limited to a few layers of the AFM Cr surrounding the FM Fe clusters.

4 A purely cluster-composed material: Iron-Scandium nanoglasses

In this chapter experiments and results obtained on amorphous Fe-Sc clusters are presented and discussed. In recent years, the discovery of a possible new type of amorphous state in metallic glasses has been reported. This new state is characterized by a significantly reduced density and displays markedly different magnetic properties, compared to those of rapidly quenched amorphous alloys of the same composition. Specifically, the new amorphous state is formed during compaction of preformed amorphous Fe-Sc nanoparticles. In order to gain additional evidence on this possibly new amorphous state, while at the same time to further exploit the capabilities of the new cluster deposition system, Fe-Sc clusters were deposited, using the first deposition stage of the system (Chap. 2.4.1). The results that were obtained on the synthesized material not only yielded new evidence and insights on the details of the new amorphous state, but they also indicated that the new deposition system is an effective and suitable tool to conduct future research on the topic of nanoglasses.

4.1 Motivation and introduction

The first metallic glass or amorphous metal was synthesized in 1960 by Klement, Willens and Duwez [41] by rapidly quenching $Au_{75}Si_{25}$ from the melt. Since then, numerous metallic glasses were synthesized mainly using new quenching techniques that allowed for higher cooling rates or, alternatively, by utilizing more complex alloy systems, where lower cooling rates are sufficient to achieve full amorphization. Nevertheless, most materials thus synthesized are limited to rather thin layers, in the range of 20 to 50 micrometers. In addition in a few alloy systems, typically consisting of three or more components, the cooling rates can be low enough for the material to be synthesized with thicknesses far greater than a millimeter. Due to the rather large material thicknesses, one refers to these materials as bulk metallic glasses. Except for thin films, that can be synthesized, for example by PVD techniques, metallic glasses are typically still prepared by rapid

quenching from the melt. Consequently, the only parameters that allow for influencing the final glass structure within a limited range, are the quenching rate and the starting temperature of the quenching process. Accordingly, in all melt-spun metallic glasses, the short and medium range order, the density, and the chemical composition are determined by the corresponding parameters that cannot be modified over a wide range, but just by a few percent.

Recently a new type of metallic glass has been discovered, which is referred to as nanoglass [42]. Differently from conventional metallic glasses, prepared by rapid quenching, the nanoglasses are typically prepared by the consolidation of nanometer-sized, amorphous nanoparticles that were previously produced by the inert gas condensation method (IGC). The presently available experimental data seem to indicate, that at the interfacial regions, delimiting the primary nanoparticles after their consolidation, a new amorphous phase with its own distinct characteristics is formed. This new state is characterized by the presence of a substantially increased free volume (reduced density) as well as physical properties (e.g. magnetic, mechanical etc.) that are significantly different from those of the rapidly quenched amorphous alloys or even the primary nanoparticles having the same composition as the nanoglass [43–45].

The amorphous Fe-Sc alloy (90 at.% Fe, 10 at.% Sc), which has been extensively studied by our group at the Institute of Nanotechnology, can be used as an illustrative example of this new nanoglass state. ^{57}Fe Mössbauer spectroscopy (MS) conducted on the above alloy revealed, that the new amorphous state is formed at the interfacial regions between the primary nanoparticles after their consolidation, having a volume fraction of about 35 % for average sizes of the primary particles of $\approx$ 8 nm [45]. Moreover, the new amorphous state is stable at room temperature (RT) and it is characterized by a reduced density of up to 17 % [43], compared to the core of the primary nanoparticles. It is important to restate here, that this unique and new state is neither found in the primary nanoparticles nor in rapidly quenched amorphous Fe-Sc of the same composition [46]. Furthermore, it is important to note that the Fe-Sc nanoglass is FM at RT, while rapidly quenched amorphous Fe-Sc, of any composition, and the non-consolidated primary nanoparticles are PM at RT [47]. Indeed, the highest Curie temperature of any amorphous Fe-Sc alloy over the entire compositional range is 230 K [47]. MS and a variety of other characterization techniques confirm that a nanoglass consists of two distinct amorphous regions, one in the cores of the former nanoparticles, and one in the interfacial regions between these cores. The core regions are clearly distinguished from the interfacial regions by their density, chemical composition and magnetic properties. Molecular dynamics simulations, conducted by Şopu et al. [48] showed, that the structural features of the nanoglasses, that is the regions

with reduced density between the cores of the primary nanoparticles, can be reproduced by assuming amorphous nanospheres with 5 nm in diameter, that are joined together under high pressure. A more descriptive explanation on the formation of the new amorphous state is as follows: small pores or voids are left behind between the primary nanoparticles, after the consolidation step, as it would be the case for an assembly of hard spheres. These voids (pores) are then filled by atoms diffusing from the outmost regions of the primary nanoparticles, which become thereby partly dissolved. Following this explanation it is obvious, that the consolidation step as well as the primary particle size are both very important factors for the formation of this new amorphous phase: the consolidation step mainly determines the overall volume of the pores left in the sample. This in turn, basically determines an upper limit for the volume percent of the new phase that can be formed, whereas the primary particle size influences the size of the single pores as well as the fraction of atoms in the contact areas (necks) between the primary nanoparticles, being both important for the ensuing diffusion process that follows.

To date, the IGC method and the subsequent compaction step, together constitute the most appropriate technique for synthesizing nanoglasses. Using this technique the size of the amorphous primary nanoparticles can be roughly obtained in the range from 7 nm to 20 nm adjusting the evaporation rate and the inert gas pressure in the vacuum chamber. However, since no option is available for monitoring the size of the nanoparticles during synthesis, it can only be obtained after their deposition by some appropriate technique such as, TEM. A second serious drawback of the IGC method lies in the fact, that it typically uses a thermal evaporation process. This makes the investigation of alloy systems, consisting of elements with different vapor pressures, difficult and consequently, the number of material systems that can be prepared is rather limited. Therefore, in order to be able to synthesize nanoglasses in a more controlled manner so as to gain additional information about the properties of the new amorphous state, as well as to proceed on the way to the final goal of being able to synthesize the new state as a pure phase, the new CIBD system was used to carry out a series of experiments. Compared to the IGC systems it has many advantages:

Straightforward adjustment of the primary particle size: the average particle size produced by the source can easily be adjusted by a set of source parameters (e.g. sputter power, aggregation gas pressure and gas mixture) from some tens of atoms per cluster up to clusters with several nm in diameter. In addition, the produced cluster size is monitored by the TOF. This makes it possible to control the synthesis process so that series of samples, with different and well-defined (targeted) particle sizes can be produced.

Magnetron sputtering instead of thermal evaporation: in contrast to most available IGC systems, magnetron sputtering is used in combination with the inert gas condensation instead of thermal evaporation. Therefore the chemical composition of the synthesized nanoparticles is mostly (preferential sputtering) defined by the starting composition of the sputtering target and more complicated material systems (with elements having distinctly different vapor pressures) can be used.

The nanoparticle synthesis is decoupled from deposition: since the deposition process in the CIBD system is decoupled from the production of the precursor nanoparticles, the synthesis of the consolidated amorphous structure can take place under UHV conditions. This has the effect of preventing both, oxidation of the sample as well as the incorporation of gases (used for the IGC process) in the sample.

A more flexible compaction step: in the CIBD system the consolidation of the nanoparticles/clusters is achieved by means of their impact energy, instead of mechanical compaction, which can be adjusted over a wide range from 10 eV up to 12 keV per cluster. Assuming that clusters hitting the surface are completely stopped within one cluster diameter the pressure occurring during the impact can be estimated. For a particle with 1.5 nm radius (corresponding to roughly 1000 Fe atoms) one obtains a pressure range of roughly 10 MPa to 100 GPa. Therefore, this covers a considerably wider range of pressure values than those that can be obtained via the mechanical compression units that are commonly used in conventional IGC systems (typically limited to a few GPa).

4.2 Experimental details

In the previously examined materials systems Fe/Ag and Fe/Cr, where Fe clusters were embedded into an Ag and Cr matrix, the focus of the experiments was on the size-dependent properties and consequently, it was essential to closely control the size of the clusters and to obtain a narrow cluster size distribution. For the synthesis of nanoglasses by impact of amorphous clusters onto a substrate with controlled energy, clusters having the size distribution directly behind the source (Fig. 2.3) of the CIBD system can be employed, and the first deposition stage was used for the experiments (Chap. 2.4.1). With the drawback of the broader size distribution, the essential benefit of using the first deposition stage for the experiments with Fe-Sc is the fact that larger amounts of clusters can be deposited in relatively short times (in the order of an hour), compared to the size-selected deposition in the second stage.

The larger amounts of clusters (purely cluster-composed thin films with thicknesses of roughly 100 nm) allow for studying the samples with MS as well as conducting measurements of the mechanical properties and others in the future.

In general, when synthesizing metallic glasses, a fast transition from the liquid to the solid phase is beneficial, since it promotes the formation of the amorphous phase. For eutectic compositions, the liquid phase is typically maintained to low temperatures and the transition occurs in a very narrow temperature range, hence such compositions are well suited for glass-formation. Fe-Sc has two eutectic compositions, one on the Fe-rich side (89.8 at.% Fe, 10.2 at.% Sc) and one on the Sc-rich side (24.9 at.% Fe, 75.1 at.% Sc) of the binary phase diagram [49]. In a previous study carried out in our group the magnetic properties of Fe-Sc nanoglasses, with roughly 90 at.% Fe, close to the eutectic point on the Fe-rich side were investigated [45]. In these samples, used in the study, roughly 10 % of the Fe was typically present as α-Fe. Hence, in order to synthesize the Fe-Sc alloy without the presence of the α-Fe phase, a composition, containing only 80 at.% Fe (but still close to the eutectic composition) was chosen for the experiments with the new CIBD system.

A series of three samples, with an average cluster size of 1000 atoms/cluster ($\pm$300 atoms, determined by the TOF) and deposited with impact energies of 600 eV, 900 eV, and 12 keV per cluster, respectively, was synthesized using the first deposition stage in the CIBD system. From this point on, the three samples in the series will be respectively referred to as the 600 eV, 900 eV, and 12 keV sample. For all the samples, an Si substrate with its native oxide layer was used. Furthermore, the thin film samples were protected against oxidation with a 10 nm thick titanium capping layer after deposition of the clusters. The deposition time for the Fe-Sc cluster layer was roughly 1 h for each sample, resulting in film thicknesses of the order of 100 nm (as measured with a profilometer).

4.3 Results and discussion

In the previous experiments with Fe-Sc nanoglasses prepared by the IGC method, it was shown that one of the fingerprint characteristics of the new amorphous phase (present in the interfaces between the primary nanoparticles) is, that it is FM at RT. Hence, the magnetic properties of the film samples prepared with the CIBD system, were studied using a SQUID magnetometer. Moreover, the film samples were also studied with MS in order to obtain additional information, on a local scale, about the samples together with getting a better understanding of the type of material being formed along with the corresponding volume fractions (rapidly quenched-like or nanoglass). Finally, in order to verify that the samples are amorphous,

their structure was determined by TEM and X-ray diffraction (XRD). The results are discussed in the following sections.

4.3.1 Structural analysis: TEM and XRD

Figure 4.1 shows representative TEM micrographs of the 600 eV (a) and the 12 keV (b) samples. In both samples, the material is clearly amorphous, with the exception of a negligible fraction of crystallites with approximately 2 nm diameter that were found in some of the micrographs. These crystallites might have formed when parts of the sample surface were unprotected, during or after preparation of the samples for TEM. As it is discussed in the following sections, this assumption is strengthened by the fact that in none of the displayed samples any indication of Fe oxides or α-Fe was detected in the MS measurements.

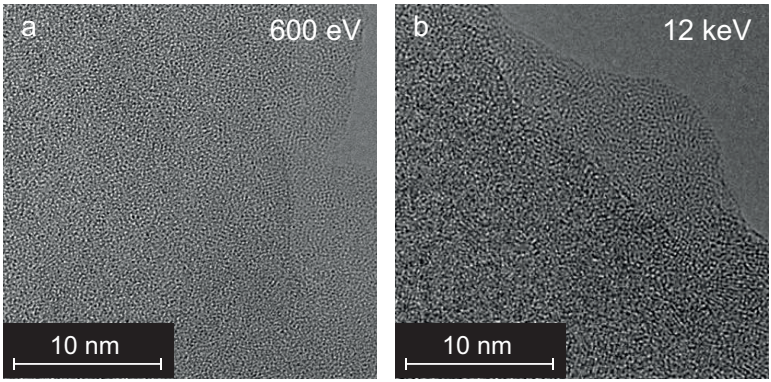

Figure 4.1.: Transmission electron microscopy (TEM) micrographs of Fe-Sc samples prepared by deposition of amorphous Fe-Sc alloy clusters with 1000 atoms on a Si/SiO_2 substrate. (a) Micrograph of the 600 eV sample. (b) Micrograph of the 12 keV sample. Besides a minute fraction of small crystallites, both samples are fully amorphous.

In order to obtain additional confirmation that the samples are amorphous, XRD was performed of the 600 eV and the 12 keV samples. The XRD patterns were obtained using a grazing incidence geometry with an incident angle of 0.5° and Cu-K_α radiation. The XRD patterns are shown in figure 4.2. In both diffraction patterns a broad intensity maximum around $2\theta \approx 44°$ is present. Its position perfectly matches that for Fe-Sc for the chemical composition used in the present

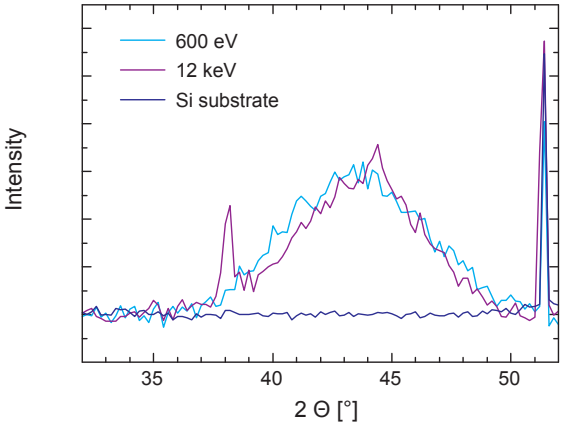

Figure 4.2.: X-ray diffraction of Fe-Sc samples recorded in grazing incidence with an incident angle of 0.5°. The 600 eV sample as well as the 12 keV sample are clearly amorphous. Additional sharp reflections in the diffraction patterns can be assigned to the Si substrate (both samples) and the Ti protection layer (12 keV sample), respectively.

experiments and its large width, of almost 5° is clearly indicating an amorphous structure. The additional sharp reflections, being visible in the two patterns, indicate the presence of crystalline material. They can be assigned to the Si substrate (in both the 600 eV and the 12 keV sample) and the Ti capping layer, whereas the Ti reflections are only visible in the diffraction pattern of the 12 keV sample. The fact, that they are not visible in the diffraction pattern of the 600 eV sample might indicate a higher surface roughness, on a small lateral scale, of this sample compared to the other sample.

From the TEM and XRD measurements it is evident that both samples are fully amorphous, but within the resolution of these two methods it is not possible to detect any differences in the amorphous structure of the high and low impact samples.

4.3.2 Magnetic characterization

For the magnetic characterization of the samples, ZFC/FC curves in a temperature range from 10 K to 390 K as well as magnetization loops at 5 K and 300 K were measured for the three samples. The measurement geometry was in-plane for all measurements, this means that the external magnetic field was applied parallel to the sample surface.

The ZFC/FC measurements are presented in figure 4.3. From the measurements it can be seen, that all three samples undergo a FM to PM transition, which is shifted to distinctly higher temperatures for lower deposition energies.

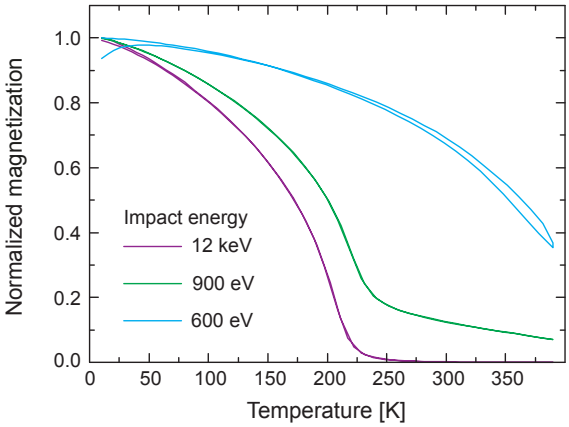

Figure 4.3.: Zero field cooled/field cooled (ZFC/FC) magnetization measurements of Fe-Sc samples, prepared with different impact energies and a cluster size of roughly 1000 atoms. While the 12 keV sample displays a ferromagnetic to paramagnetic (FM to PM) transition temperature at about 200 K, the 600 eV sample, instead, is still FM at room temperature (RT). The 900 eV sample displays a magnetic behavior somewhat in between the two other samples. According to the binary magnetic phase diagram, amorphous Fe-Sc, of any composition, is PM at temperatures above 230 K.

The 12 keV sample undergoes the FM to PM transition around 200 K and is almost totally PM for temperatures above 250 K. For the 900 eV sample the transition is also clearly visible, but it is shifted to slightly higher temperatures (around 250 K). Furthermore, this sample shows the presence of a small FM component

even at RT. The FM to PM transition temperature is distinctly shifted in the 600 eV sample. In this sample it is above 400 K and therefore above the measurement region of the used magnetometer.

Figure 4.4 shows the magnetization loops of the three samples that were measured at 5 K and 300 K. At 5 K, all three samples are FM and the material is easy to be saturated with nearly no coercivity. This behavior is perfectly consistent with the magnetic phase diagram for amorphous Fe-Sc. However, the magnetization loops measured at 300 K display some distinct differences among the three samples:

600 eV (Fig. 4.4 a): the sample is FM at 300 K and the magnetic moment is similar to the moment measured at 5 K and it is easy to saturate. The main difference in the magnetization loop measured at 300 K, compared to the loop measured at 5 K, is a loss of about 25 % in saturation magnetization.

12 keV (Fig. 4.4 c): at 300 K no FM component is present in the magnetization loop. The loop has nearly a linear shape and at this temperature the sample seems to be (mostly) PM. Regarding the ratio of the FM moment at 5 K to that of the PM moment at 300 K, it is very much close to the ratio of that of the Fe-Sc melt-spun ribbons, reported by Ryan et. al. [50].

900 eV (Fig. 4.4 b): this sample shows a magnetic behavior that appears to be a mixture of the other two samples. On one hand, it features a weak FM component at 300 K that is roughly 10 % of its saturation magnetization value at 5 K. On the other hand, the PM component is hard to saturate. Finally, the shape of the PM component in the magnetization loop is similar to that of the 12 keV sample.

Comparing the above magnetic results to the previous results obtained on the Fe-Sc nanoglasses that were prepared by the IGC method as well as those reported on rapidly quenched amorphous Fe-Sc, magnetically, the 12 keV sample resembles to rapidly quenched amorphous Fe-Sc of the same composition [46]. The FM to PM transition is in a similar temperature range and the 12 keV sample is, as rapidly quenched amorphous Fe-Sc, purely PM at RT. By way of contrast, the FM character of the 600 eV sample persists at 300 K and even at higher temperatures. This result can not be explained on the basis of the magnetic phase diagram of amorphous Fe-Sc prepared by PVD. Instead, the magnetic characteristics of this sample resemble to those of the interfacial regions appearing to be present in the Fe-Sc nanoglass of similar chemical composition [45].

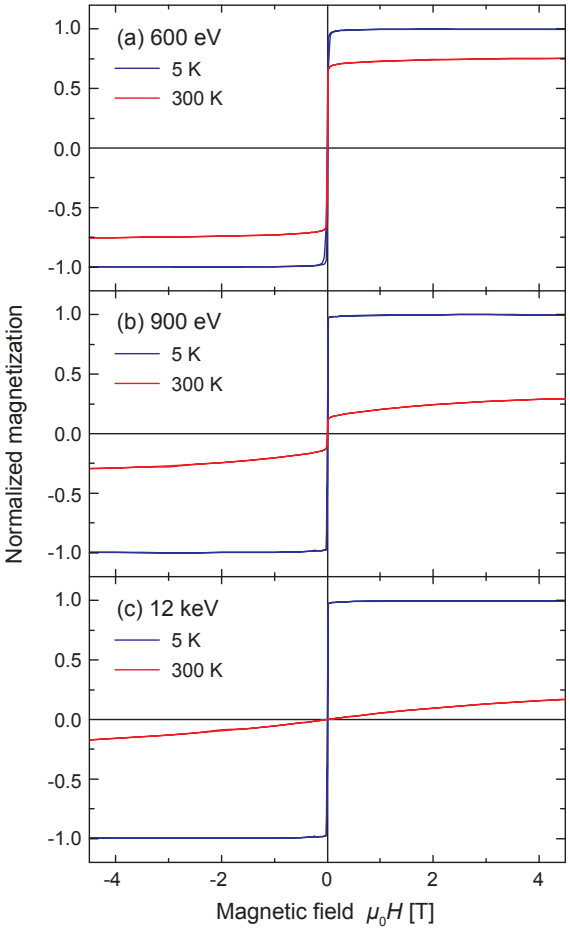

Figure 4.4.: Magnetization loops of Fe-Sc samples measured at 5 K and 300 K. At 5 K the three samples are ferromagnetic (FM) and the material is easy to saturate. At 300 K distinct differences among the three samples are present. The 600 eV sample (a) is still FM at 300 K and it looses roughly 25 % of the 5 K saturation magnetization value. By contrast, the 300 K magnetization loop of the 12 keV sample (c) is almost linear, implying that the sample is (mostly) paramagnetic (PM) at 300 K. At this temperature the 900 eV sample (b) has both a FM and a PM component.

4.3.3 ^{57}Fe Mössbauer spectroscopy

In order to characterize the samples with MS and thereby obtaining local information about the surrounding and the electronic and chemical state of the individual Fe atoms in the sample, Conversion Electron Mössbauer Spectroscopy (CEMS) was performed at RT and at 80 K for both the 12 keV and the 600 eV samples. By fitting histogram distributions to the individual spectra the relevant MS parameters were derived:

Magnetic hyperfine field (B_{HF}): from the presence of the magnetic hyperfine splitting B_{HF} and the determined value, information about the local magnetic order (e.g. FM or PM) can be derived.

Quadrupole splitting (QS): the QS yields information about the local symmetry of the charge distribution around the Fe nuclei.

Isomer shift (IS): the IS is determined by the local chemistry and it yields information about the charge (electronic) state of the individual Fe atoms.

Furthermore, by fitting the histogram distributions to the MS spectra possible sub-spectra can be identified. From the relative areas of the sub-spectra, the fractions of Fe atoms being in a certain electronic and magnetic state can be derived.

Figure 4.5 a shows a RT MS spectrum of the 12 keV sample. The spectrum only consists of a single component, being that of a quadrupole doublet, indicating a paramagnetic state, which fits quite well to the information that was obtained from the magnetic data of the sample and to MS spectra obtained from rapidly quenched samples of the same composition. In contrast, the MS spectrum of the 600 eV sample (Fig. 4.5 b) shows a magnetic sextet, confirming that the sample is FM at RT (as it was already indicated by the magnetometric). For the purpose of comparison, the MS spectrum of a nanoglass, produced by the IGC method (90% Fe), used in previous experiments is also shown (Fig. 4.5 c). This latter spectrum features both a quadrupole doublet and a sextet. In an aforementioned previous publication on Fe-Sc nanoglasses [45], the two components being in the MS spectrum (doublet, sextet), were explained by assuming that the IGC samples consist of two distinctly different amorphous phases: one component representing the former cores of the compacted primary nanoparticles, that is similar to rapidly quenched amorphous alloys, and consequently PM at RT and a second component, the interfacial regions, that is FM at RT.

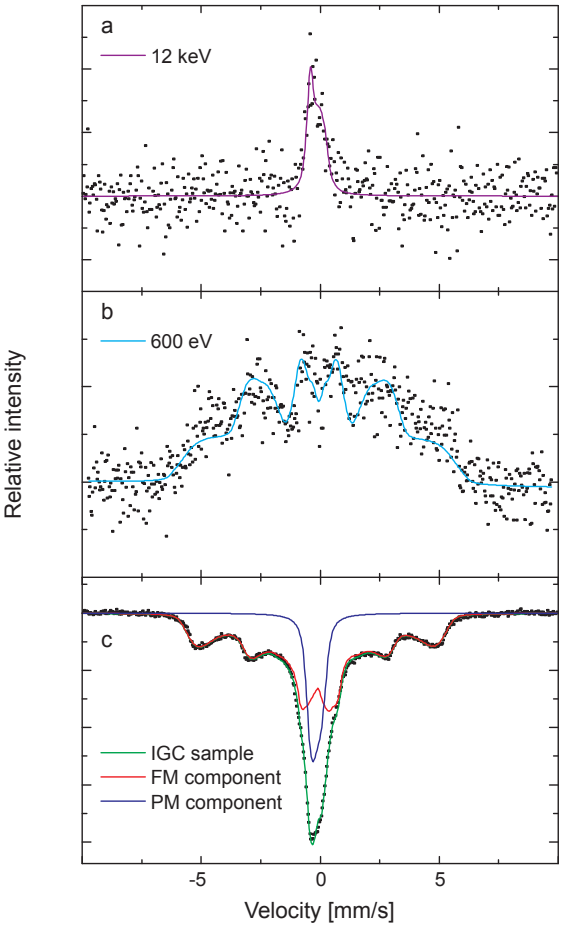

Figure 4.5.: Mössbauer spectra of Fe-Sc samples recorded at room temperature (RT). The solid lines represent fits to the data. The spectrum of the 12 keV sample (a) shows a quadrupole doublet. By contrast, the spectrum of the 600 eV sample (b) shows a magnetic sextet. For comparison in (c) a MS spectrum of a sample prepared by the inert gas condensation (IGC) method with 90 atomic percent (at.%) Fe is shown. This latter spectrum features both, a quadrupole doublet and a sextet. The differences of the signs of the line intensities are due to different measurement modes and the statistics of (c) is better due to larger amounts of material being used for the measurement.

At 80 K both the MS spectrum of the 12 keV sample (Fig. 4.6 a) and the MS spectrum of the 600 eV sample (Fig. 4.6 b) feature a FM sextet. This observation is consistent with the results obtained from the magnetic data taken on the two samples. The magnetic data revealed that both samples are FM below 200 K. However, the distinct difference between the FM sextets in the MS spectra of the two samples is their relative width, that is (the width) described by the distributions of B_{HF} (Fig. 4.6 c), obtained from histogram distributions fitted to the data. The spectrum of the 12 keV sample has only a single distribution of B_{HF}, with an average value of around 11 T. By contrast, the spectrum of the 600 eV sample, features a similar distribution of B_{HF} at low fields, and an additional, by far dominant one, around 30 T. Regarding the areas of the two distributions of B_{HF} in the spectrum of the 600 eV sample, the area of the distribution around 30 T is roughly four times larger than the area of the distribution around 11 T. This can be interpreted as meaning that roughly 20 % of the Fe atoms in the 600 eV sample are in a similar surrounding as the Fe atoms in the 12 keV sample, while the remaining 80 % of the atoms are in a different surrounding, which might that of the postulated new interface phase.

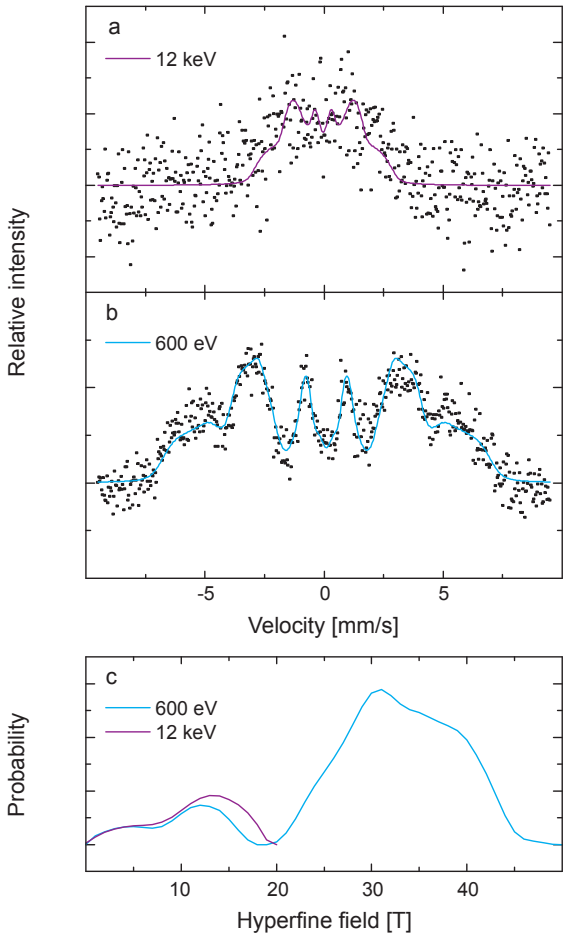

Figure 4.6.: Mössbauer spectra of Fe-Sc samples recorded at 80 K. The solid lines are fits to the data. While the spectrum of the 12 keV sample (a) shows a weakly split sextet, the spectrum of the 600 eV sample is dominated by a sextet with large splitting. In (c) is shown the distribution of the magnetic hyperfine fields (B_{HF}) of the two samples (for clarity the probability axis of the B_{HF} was rescaled). While the spectra of both samples show a distribution of B_{HF} around 11 T, the spectrum of the 600 eV sample features an additional, dominant distribution around 30 T, representing approximately 80 % of the ^{57}Fe atoms.

The MS parameters, obtained from fitting the histogram distributions to the MS spectra of the 12 keV sample and the 600 eV sample are summarized in table 4.1. For comparison MS parameters for the RT MS spectrum of an IGC-prepared nanoglass (Fig. 4.5 c), are also included in the table.

Table 4.1.: Mössbauer spectroscopy (MS) parameters obtained from fitting histogram distributions to the MS spectra of the 12 keV and the 600 eV samples. The $\langle CS \rangle$ is the average central shift, which is composed of the sum of the average isomer shift plus contributions from 2nd order Doppler shift; it is given relative to the $\langle CS \rangle$ of metallic Fe at room temperature (RT).

	$\langle CS \rangle$ [mm/s]	$\langle QS \rangle$ [mm/s]	$\langle B_{HF} \rangle$ [T]
RT			
12 keV	-0.09(2)	0.41(2)	
600 eV	0.04*		22(1)
IGC PM	-0.08(1)	0.39(2)	
IGC FM	-0.02(1)		18(1)
80 K			
12 keV	0.07*		11
600 eV	0.20(1)		30

At RT the average central shift $\langle CS \rangle = -0.09(2)$ mm/s of the 12 keV sample is within its error the same as the $\langle CS \rangle$ of the PM component of the IGC-prepared nanoglass, and perfectly fits to data that can be found in the literature on rapidly quenched amorphous alloys of the same chemical composition [46]. The same is true for the average quadrupole splitting $\langle QS \rangle$. Therefore it can be stated, that the 12 keV sample is resembling rapidly quenched Fe-Sc alloy of the same chemical composition.

Since the RT data of the 600 eV sample were rather noisy, it was not possible to obtain a reliable value for the $\langle CS \rangle$. Therefore, it was kept constant in the fit and its value, close to zero, was deduced from the 80 K data. The low value is similar to what is expected for metallic Fe. This is a clear indication that no oxides are present in the sample, and a confirmation that the oxides observed in TEM are indeed a result of the sample preparation instead of being present in the protected sample.

As already mentioned, in the RT MS spectrum of the 600 eV sample just one component is visible (as for the 12 keV sample). The deduced $\langle B_{HF} \rangle$ is clearly higher than that of the IGC-prepared sample.

At 80 K the $\langle CS \rangle$ of both the MS spectrum of the 12 keV sample and that of the 600 eV sample are shifted to more positive values compared to the corresponding RT data. This is due to contributions of 2nd order Doppler shifts. The $\langle B_{HF} \rangle = 11$ T obtained for the 12 keV sample at 80 K is again perfectly matching the already mentioned data on rapidly quenched amorphous Fe-Sc [46], while the $\langle B_{HF} \rangle = 30$ T is nearly three times higher.

4.3.4 Discussion

In summary, the data obtained from the various measurements on the 12 keV cluster-deposited Fe-Sc sample revealed that:

1. the sample is totally amorphous;

2. the sample is PM at temperatures above 230 K, while being FM at temperatures below 230 K;

3. the MS parameters are identical with the ones of rapidly quenched amorphous Fe-Sc of the same composition.

Therefore, it can be stated, that the sample perfectly resembles the characteristics of rapidly quenched amorphous Fe-Sc. This result might be explained by the high impact energy, of roughly 12 eV/atom, which has the effect of destroying the clusters when they land. Furthermore, the heat induced by the impact of the clusters can be immediately distributed within the substrate and the growing thin film. Thus, at high impact energies, the process is basically similar to that during rapid quenching.

The situation is completely different for the case of the 600 eV sample. With this deposition energy, the sample remains FM at RT and even above, an effect, that was already found for the interfacial regions of the IGC-prepared nanoglasses of a similar chemical composition. It is beyond any doubt, that the binary magnetic phase diagram of amorphous Fe-Sc can not account for the FM behavior observed at RT both in the IGC-prepared nanoglasses and in the 600 eV sample. Therefore, the FM behavior at RT might be explained on the basis of a new amorphous phase being formed, as it is assumed to be the case for the IGC-prepared nanoglass. However, other possible explanations for the FM behavior at RT need to be excluded, namely, the formation of either α-Fe and/or Fe oxide (Fe_2O_3) in the sample and a part of the

sample exhibiting a crystalline instead of an amorphous structure. In the following paragraphs, arguments are presented to exclude these alternative explanations.

α-Fe: α-Fe in the sample could also result in the sample displaying a FM behavior at RT. α-Fe would cause a sharp sextet in the MS spectra, the positions of which are indicated in figure 4.7. Such peaks would be clearly visible in the broad distribution featured by the 600 eV sample at RT and at 80 K. Therefore, the presence of a noteworthy percentage of α-Fe in the sample that would be sufficient to account for the strong FM behavior of the sample at RT can be excluded.

Fe_2O_3: Fe oxides in the sample could also explain the FM at RT. However, in that case one would either expect a sharp sextet or a sharp doublet (depending on the magnetism) in the RT MS spectrum. The positions of the peaks belonging to the sextet and the doublet, respectively, are shown in figure 4.7. Since no sharp peaks are found at the corresponding positions (not at all), as for the case of α-Fe, a considerable amount of Fe_2O_3 in the sample should be present to account for the FM behavior at RT. Since no such amount was detected, this hypothesis can, therefore, also be excluded.

Crystalline samples: if the samples would be crystalline instead of amorphous they could also feature different kinds of magnetism. However, noteworthy amounts of crystalline material in the samples can be excluded, since a hint for a sufficient amount of crystalline material to explain the strong RT FM was neither found in the TEM micrographs nor in the XRD pattern. In particular, the XRD patterns only showed a broad intensity maximum, clearly indicating an amorphous structure. Sharp reflections originating from crystalline Fe, Sc or Fe_2-Sc were definitely not present at their respective positions in the XRD patterns.

Therefore, any kind of magnetic "contamination" can be excluded and the only remaining plausible explanation for the RT FM observed in the 600 eV sample is the formation of the postulated new amorphous phase. In addition to the magnetometric data measured on the 600 eV sample, the obtained MS parameters indicate similar characteristics of the local ^{57}Fe surrounding as those for the new amorphous interfacial phase in the IGC-prepared nanoglass. Furthermore, as previously mentioned, at 80 K, the 600 eV sample exhibits two distributions of $\langle B_{\mathrm{HF}} \rangle$, as shown in figure 4.6 c. First, a smaller one around $\langle B_{\mathrm{HF}} \rangle = 11$ T, with roughly 20 % relative area, being comparable to the one expected for an amorphous thin film and the 12 keV sample. And, secondly, a larger one, around $\langle B_{\mathrm{HF}} \rangle = 30$ T, with roughly

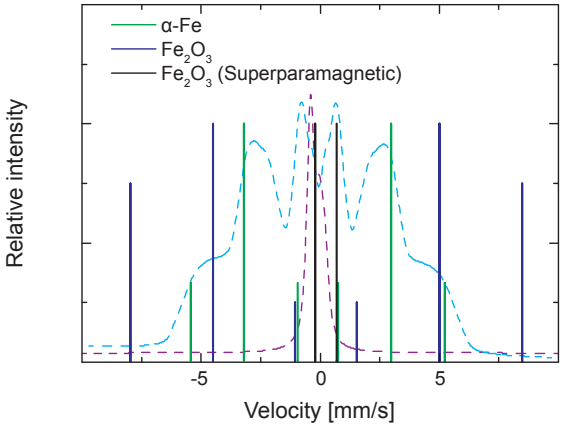

Figure 4.7.: Peak positions in the Mössbauer spectra of possible contaminations of Fe-Sc samples. The simulated peaks represent the most possible magnetic contaminations: α-Fe and FeO.

80 % relative area, indicating the presence of the new amorphous phase. For the IGC-prepared nanoglasses, the new amorphous phase was shown to represent up to 35 % of the whole material [45]. Here, for the 600 eV sample, the relative areas of the two distributions of B_{HF} in the 600 eV sample indicate the formation of the new amorphous phase up to a fraction of 80 % of the whole material.

Assuming that, as for the nanoglasses prepared by IGC, the new amorphous phase is formed in the interfaces between the primary nanoparticles, the high percentage of the new amorphous phase of 80 % in the 600 eV sample might be explained as follows. The deposition energy was 600 eV per cluster, corresponding to 0.6 eV/atom, approximately fulfilling the conditions for soft landing of the clusters. Therefore, one can assume, that the clusters stay relatively intact during landing and, that the clusters are stacked on top of each other rather loosely, with a lot of voids being left among the contiguous clusters. In addition, the cluster size of 1000 atoms/cluster, corresponds to a cluster diameter of roughly 3 nm, which also roughly defines the size of the voids among the stacked clusters to be in a similar range. Hence, many voids are left in the sample after cluster deposition that, due to their small dimensions, can be easily filled by atoms originating from the cores of the clusters, which are thereby partly dissolved, and a large amount of the new phase can be formed in the interfacial regions of the cluster assembly.

4.4 Conclusions

In conclusion, systematic experiments on Fe-Sc nanoglasses were conducted using the new CIBD system. For this first series of experiments, a single cluster size was used, namely 1000 atoms/cluster and different compaction scenarios were mimicked, by varying the impact energy of the clusters.

The experiments revealed that using high impact energies of several eV/atom, an amorphous material can be formed, that is closely corresponding to rapidly quenched material of the same chemical composition. Therefore, it can be stated that, in future experiments with different alloy systems, it will be possible to reliably synthesize reference samples representing rapidly quenched amorphous material by depositing clusters with high impact energies.

Different from the high impact energy case, it was shown that, using low impact energies of the order of 0.5 eV/atom, a new amorphous phase can be formed that accounts for roughly 80 % of the resulting cluster-based material. This fraction of the new amorphous phase is far higher than the reported 30 % for IGC-prepared nanoglasses [45]. Furthermore, in contrast to the IGC-prepared nanoglasses, the amorphous iron-scandium prepared by cluster impact with low energy is completely ferromagnetic at room temperature.

To date, the experiments on Fe-Sc are ongoing, and their focus is to synthesize the new amorphous phase to higher percentages or even phase-pure, by further varying the deposition parameters or the size of the primary clusters. The deposition energy can still be lowered by a factor of sixty, down to 10 eV/cluster, and the cluster-size can be lowered by a factor of ten down to 100 atoms/cluster. Consequently, a substantial research effort still remains to be carried out by exploiting the capabilities of the new CIBD system.

5 Summary and future work

In the course of this thesis a versatile ultra-high vacuum apparatus for the fine-tuned synthesis of cluster-assembled nanomaterials has been designed and constructed based on a detailed simulation of the ion optics. Using the numerous options of the system for adjustment and control of the experimental parameters, a wide variety of compositions and morphologies of cluster-assembled materials can be readily prepared.

The performance parameters of the system were tested using an immiscible alloy system consisting of iron clusters embedded in a silver matrix. A remarkably high degree of precision and control in terms of sample homogeneity, fraction of clusters and reproducibility was demonstrated, which was, to that degree, never reported in the literature.

In a series of experiments with iron clusters embedded in a chromium matrix the magnetic characteristics of the material system were studied. Benefiting from the high degree of control of the deposition parameters during the synthesis a large series of consistent samples was prepared to give a clear insight into the correlation between the sample morphology (e.g. size and volume fraction of the embedded clusters) and the magnetic properties.

In a second series of experiments a so-called nanoglass based on amorphous iron-scandium alloy clusters was studied. The results indicate the formation of a new amorphous structure that exhibits ferromagnetism above room temperature. In contrast, a rapidly quenched amorphous alloy of identical composition is paramagnetic at temperatures above 230 K. The distinct difference in magnetism of chemically identical amorphous alloys is an evidence for a novel atomic structure existing in cluster-assembled glasses.

Both series of experiments show that the experimental capabilities provided by the newly developed cluster deposition system allow contributions to various fields of cluster-assembled materials. Future research will address the synthesis and characterization of additional cluster/matrix combinations and nanoglasses, and the preparation of model systems for nanocatalysis.

Bibliography

[1] E. Barborini, G. Corbelli, G. Bertolini, P. Repetto, M. Leccardi, S. Vinati, and P. Milani, New Journal of Physics **12**, 073001 (2010) 10.1088/1367-2630/12/7/073001 (cit. on p. 1).

[2] S. H. Baker, M. Roy, S. C. Thornton, and C. Binns, Journal of physics. Condensed matter : an Institute of Physics journal **24**, 176001 (2012) 10.1088/0953-8984/24/17/176001 (cit. on p. 1).

[3] J. Bansmann, S. Baker, C. Binns, J. Blackman, J. Bucher, J. Dorantedavila, V. Dupuis, L. Favre, D. Kechrakos, and A. Kleibert, Surface Science Reports **56**, 189 (2005) 10.1016/j.surfrep.2004.10.001 (cit. on p. 1).

[4] C. Binns, S. Baker, S. Louch, F. Sirotti, H. Cruguel, P. Prieto, S. Thornton, and J. Bellier, Applied Surface Science **226**, 249 (2004) 10.1016/j.apsusc.2003.11.069 (cit. on p. 1).

[5] V. Dupuis, L. Favre, S. Stanescu, J. Tuaillon-Combes, E. Bernstein, and A. Perez, Journal of Physics: Condensed Matter **16**, S2231 (2004) 10.1088/0953-8984/16/22/024 (cit. on p. 1).

[6] B. Palpant, B. Prével, J. Lermé, E. Cottancin, M. Pellarin, M. Treilleux, A. Perez, J. Vialle, and M. Broyer, Physical Review B **57**, 1963 (1998) 10.1103/PhysRevB.57.1963 (cit. on p. 1).

[7] S. Kunz, K. Hartl, M. Nesselberger, F. F. Schweinberger, G. Kwon, M. Hanzlik, K. J. J. Mayrhofer, U. Heiz, and M. Arenz, Physical chemistry chemical physics : PCCP **12**, 10288 (2010) 10.1039/c0cp00288g (cit. on p. 1).

[8] Y. Watanabe and N. Isomura, Journal of Vacuum Science & Technology A: Vacuum, Surfaces, and Films **27**, 1153 (2009) 10.1116/1.3179160 (cit. on p. 1).

[9] J. Aiken and R. Finke, Journal of molecular catalysis A: chemical **145**, 1 (1999) 10.1016/S1381-1169(99)00098-9 (cit. on p. 1).

[10] K. Bromann, C. Felix, H. Brune, W. Harbich, R. Monot, J. Buttet, and K. Kern, Science (New York, N.Y.) **274**, 956, ISSN: 1095-9203 (1996), http://www.ncbi.nlm.nih.gov/pubmed/8875931 (cit. on p. 1).

[11] H. Haberland, Journal of Vacuum Science & Technology A: Vacuum, Surfaces, and Films **10**, 3266 (1992) 10.1116/1.577853 (cit. on p. 2).

[12] X. Li, K. Wepasnick, X. Tang, D. H. Fairbrother, K. H. Bowen, A. Dollinger, C. H. Strobel, J. Huber, T. Mangler, Y. Luo, S. Proch, and G. Gantefoer, Journal of Applied Physics **115**, 104304 (2014) 10.1063/1.4868468 (cit. on pp. 3, 9).

[13] W. Krätschmer, L. D. Lamb, K. Fostiropoulos, and D. R. Huffman, Nature **347**, 354 (1990) 10.1038/347354a0 (cit. on p. 3).

[14] A. Fischer, R. Kruk, and H. Hahn, Review of Scientific Instruments **86**, 023304 (2015) 10.1063/1.4908166 (cit. on pp. 6, 9, 33, 44, 51).

[15] M. N. Blom, D. Schooss, J. Stairs, and M. M. Kappes, The Journal of chemical physics **124**, 244308 (2006) 10.1063/1.2208610 (cit. on p. 9).

[16] S. Gibilisco, M. Di Vece, S. Palomba, G. Faraci, and R. E. Palmer, The Journal of chemical physics **125**, 084704 (2006) 10.1063/1.2337288 (cit. on p. 9).

[17] N. Domingo, D. Fiorani, A. M. Testa, C. Binns, S. Baker, and J. Tejada, Journal of Physics D: Applied Physics **41**, 134009 (2008) 10.1088/0022-3727/41/13/134009 (cit. on p. 10).

[18] H. Haberland, Journal of Vacuum Science & Technology A: Vacuum, Surfaces, and Films **12**, 2925 (1994) 10.1116/1.578967 (cit. on pp. 11, 12, 15).

[19] D. Schooss, M. N. Blom, J. H. Parks, B. v Issendorff, H. Haberland, and M. M. Kappes, Nano letters **5**, 1972 (2005) 10.1021/nl0513434 (cit. on p. 11).

[20] A. Fischer, R. Kruk, D. Wang, and H. Hahn, Beilstein Journal of Nanotechnology **6**, 1158 (2015) 10.3762/bjnano.6.117 (cit. on p. 33).

[21] L. Swartzendruber, Journal of Phase Equilibria **5**, 560 (1984) 10.1007/BF02868316 (cit. on p. 35).

[22] J. Nogués and I. K. Schuller, Journal of Magnetism and Magnetic Materials **192**, 203 (1999) 10.1016/S0304-8853(98)00266-2 (cit. on p. 39).

[23] C. Baker, S. K. Hasanain, and S. I. Shah, Journal of Applied Physics **96**, 6657 (2004) 10.1063/1.1806263 (cit. on p. 40).

[24] V. Skumryev, S. Stoyanov, Y. Zhang, G. Hadjipanayis, D. Givord, and J. Nogués, Nature **423**, 850 (2003) 10.1038/nature01687 (cit. on p. 44).

[25] W. Meiklejohn and C. Bean, Physical Review **105**, 904 (1957) 10.1103/PhysRev.105.904 (cit. on p. 44).

[26] D. Peng, K. Sumiyama, T. Hihara, S. Yamamuro, and T. Konno, Physical Review B **61**, 3103 (2000) 10.1103/PhysRevB.61.3103 (cit. on p. 44).

[27] C. Binns, M. T. Qureshi, D. Peddis, S. H. Baker, P. B. Howes, A. Boatwright, S. A. Cavill, S. S. Dhesi, L. Lari, R. Kröger, and S. Langridge, Nano letters **13**, 3334 (2013) 10.1021/nl401587t (cit. on p. 44).

[28] E. Escorcia-Aparicio, H. Choi, W. Ling, R. Kawakami, and Z. Qiu, Physical Review Letters **81**, 2144 (1998) 10.1103/PhysRevLett.81.2144 (cit. on p. 44).

[29] R. Ciprian, M. Carbucicchio, and G. Palombarini, IEEE Transactions on Magnetics **46**, 432 (2010) 10.1109/TMAG.2009.2032266 (cit. on p. 44).

[30] D. Tobia, E. Winkler, R. D. Zysler, M. Granada, H. E. Troiani, and D. Fiorani, Journal of Applied Physics **106**, 103920 (2009) 10.1063/1.3259425 (cit. on p. 45).

[31] B. Kuerbanjiang, U. Wiedwald, F. Haering, J. Biskupek, U. Kaiser, P. Ziemann, and U. Herr, Nanotechnology **24**, 455702 (2013) 10.1088/0957-4484/24/45/455702 (cit. on p. 45).

[32] M. Qureshi, S. Baker, C. Binns, M. Roy, S. Laureti, D. Fiorani, and D. Peddis, Journal of Magnetism and Magnetic Materials **378**, 345 (2015) 10.1016/j.jmmm.2014.11.065 (cit. on pp. 45, 54).

[33] B. Dieny, V. Speriosu, S. Parkin, B. Gurney, D. Wilhoit, and D. Mauri, Physical Review B **43**, 1297 (1991) 10.1103/PhysRevB.43.1297 (cit. on p. 45).

[34] D. P. Shoemaker, M. Grossman, and R. Seshadri, Journal of Physics: Condensed Matter **20**, 195219 (2008) 10.1088/0953-8984/20/19/195219 (cit. on p. 45).

[35] Z. M. Tian, S. L. Yuan, S. Y. Yin, L. Liu, J. H. He, H. N. Duan, P. Li, and C. H. Wang, Applied Physics Letters **93**, 222505 (2008) 10.1063/1.3039071 (cit. on p. 45).

[36] J.-O. Andersson and B. Sundman, Calphad **11**, 83 (1987) 10.1016/0364-5916(87)90021-6 (cit. on p. 45).

[37] L. Byeong-Joo, Calphad **17**, 251 (1993) 10.1016/0364-5916(93)90004-U (cit. on p. 45).

[38] E. Fawcett, Reviews of Modern Physics **60**, 209 (1988) 10.1103/RevModPhys.60.209 (cit. on p. 51).

[39] Ò. Iglesias, X. Batlle, and A. Labarta, Journal of Physics D: Applied Physics **41**, 134010 (2008) 10.1088/0022-3727/41/13/134010 (cit. on p. 53).

[40] E. Restrepo-Parra, J. Restrepo, J. F. Jurado, C. Vargas-Hernandez, and J. C. Riano-Rojas, IEEE Transactions on Magnetics **45**, 5180 (2009) 10.1109/TMAG.2009.2031080 (cit. on p. 53).

[41] W. Krätschmer, L. D. Lamb, K. Fostiropoulos, and D. R. Huffman, Nature **347**, 354 (1990) 10.1038/347354a0 (cit. on p. 55).

[42] J. Jing, A. Krämer, R. Birringer, H. Gleiter, and U. Gonser, Journal of Non-Crystalline Solids **113**, 167 (1989) 10.1016/0022-3093(89)90007-0 (cit. on p. 56).

[43] J. X. Fang, U. Vainio, W. Puff, R. Würschum, X. L. Wang, D. Wang, M. Ghafari, F. Jiang, J. Sun, H. Hahn, and H. Gleiter, Nano letters **12**, 458 (2012) 10.1021/nl2038216 (cit. on p. 56).

[44] M. Ghafari, S. Kohara, H. Hahn, H. Gleiter, T. Feng, R. Witte, and S. Kamali, Applied Physics Letters **100**, 133111 (2012) 10.1063/1.3699228 (cit. on p. 56).

[45] R. Witte, T. Feng, J. X. Fang, A. Fischer, M. Ghafari, R. Kruk, R. A. Brand, D. Wang, H. Hahn, and H. Gleiter, Applied Physics Letters **103**, 073106 (2013) 10.1063/1.4818493 (cit. on pp. 56, 59, 63, 65, 72, 73).

[46] M. Müller, "Magnetische und strukturelle Charakterisierung von amorphen Eisen-Scandium-Legierungen", PhD thesis (TU Darmstadt, 2004), http://tuprints.ulb.tu-darmstadt.de/411/ (cit. on pp. 56, 63, 69, 70).

[47] M. Müller, M. Ghafari, S. Banihashemei, B. Stahl, and H. Hahn, physica status solidi (a) **189**, 1043 (2002) 10.1002/1521-396X(200202)189:3<1043::AID-PSSA1043>3.0.CO;2-7 (cit. on p. 56).

[48] D. Şopu, Y. Ritter, H. Gleiter, and K. Albe, Physical Review B **83**, 100202 (2011) 10.1103/PhysRevB.83.100202 (cit. on p. 56).

[49] H. Okamoto, Journal of Phase Equilibria and Diffusion **33**, 80 (2011) 10.1007/s11669-011-9967-x (cit. on p. 59).

[50] D. Ryan, J. Ström-Olsen, and W. Muir, Physical Review B **40**, 11208 (1989) 10.1103/PhysRevB.40.11208 (cit. on p. 63).

Appendices

A Curriculum vitae (Lebenslauf)

Persönliche Daten

Name:	Arne Stephen Fischer
Geburtsdatum:	30.04.1983
Geburtsort:	Heidelberg
Staatsangehörigkeit:	deutsch
Familienstand:	ledig

Ausbildung

08/1993 – 06/2002	Hans-Thoma-Gymnasium (Lörrach)
10/2003 – 05/2009	Studium der Physik an der Ruprecht-Karls-Universität (Heidelberg)
04/2008 – 04/2009	Diplomarbeit in der Emmy-Noether-Nachwuchsgruppe von Alban Kellerbauer am Max-Planck-Institut für Kernphysik (Heidelberg), Titel: “Laser Spectroscopy on the Negative Osmium Ion”

Berufstätigkeit

05/2009 – 09/2009	Wissenschaftlicher Mitarbeiter in der Emmy-Noether-Nachwuchsgruppe von Alban Kellerbauer am Max-Planck-Institut für Kernphysik (Heidelberg)
10/2009 – 05/2015	Doktorarbeit am Karlsruher Institut für Technologie (KIT)/Institut für Nanotechnologie (INT) zum Thema der vorliegenden Dissertation
06/2015 –	Wissenschaftlicher Mitarbeiter am Karlsruher Institut für Technologie (KIT)/Institut für Nanotechnologie (INT)

Wehr / Zivildienst

09/2002 – 06/2003	Zivildienstleistender in der Fachklinik Haus Weitenau (Lörrach)

B Publications

B.1 Journal articles

Magnetic properties of iron cluster / chromium matrix nanocomposites
A. Fischer, R. Kruk, D. Wang, and H. Hahn, *Beilstein J. Nanotechnol.* **6**, 1158–1163 (2015).

A versatile apparatus for the fine-tuned synthesis of cluster-based materials
A. Fischer, R. Kruk, and H. Hahn, *Rev. Sci. Instrum.* **86**, 023304 (2015).

Measurement of the Zeeman effect in an atomic anion: Prospects for laser cooling of Os^-
A. Kellerbauer, A. Fischer, and U. Warring, and A. Kellerbauer, *Phys. Rev. A* **98**, 043430 (2014).

Evidence for enhanced ferromagnetism in an iron-based nanoglass
R. Witte, T. Feng, J. X. Fang, A. Fischer, M. Ghafari, R. Kruk, R. A. Brand, D. Wang, H. Hahn, and H. Gleiter, *Appl. Phys. Lett.* **103**, 073106 (2013).

Isotope shift of the electric-dipole transition in Os^-
A. Kellerbauer, C. Canali, A. Fischer, U. Warring, and S. Fritzsche, *Phys. Rev. A* **84**, 062510 (2011).

First Optical Hyperfine Structure Measurement in an Atomic Anion
A. Fischer, C. Canali, U. Warring, A. Kellerbauer, and S. Fritzsche, *Phys. Rev. Lett.* **104**, 073004 (2010).

Frequency control of a 1163 nm singly resonant OPO based on MgO:PPLN
P. Gross, I. D. Lindsay, C. J. Lee, M. Nittmann, T. Bauer, J. Bartschke, U. Warring, A. Fischer, A. Kellerbauer, and K.-J. Boller, *Opt. Lett.* **35**, 820-2 (2010).

Ultracold antiprotons by indirect laser cooling
A. Kellerbauer, C. Canali, A. Fischer, and U. Warring, *Hyperfine Interact.* **194**, 77-83 (2009).

High-Resolution Laser Spectroscopy on the Negative Osmium Ion

U. Warring, M. Amoretti, C. Canali, A. Fischer, R. Heyne, J. Meier, C. Morhard, and A. Kellerbauer, *Phys. Rev. Lett.* **102**, 043001 (2009).

Spectroscopy of Os^- and a route to laser-cooled negative ions

U. Warring, C. Canali, A. Fischer, and A. Kellerbauer, *J. Phys. Conf. Ser.* **194**, 152022 (2009).

B.2 Conference contributions

An apparatus for the synthesis of cluster-based materials

A. Fischer, R. Kruk, and H. Hahn, Frühjahrstagung der Deutschen Physikalischen Gesellschaft, Fachverband Metall- und Materialphysik, March 30^{th} - April 04^{th}, 2014, *Dresden*.

An apparatus for the synthesis of cluster-based materials

A. Fischer, R. Kruk, and H. Hahn, Fifth Seeheim Conference on Magnetism (SCM2013), September 29^{th} – October 3^{rd}, 2013, *Frankfurt*.

An apparatus for the synthesis of cluster-based materials

A. Fischer, H. Gleiter, and H. Hahn, Frühjahrstagung der Deutschen Physikalischen Gesellschaft, Fachverband Metall- und Materialphysik, March 10–15, 2013, *Regensburg*.

An apparatus for the synthesis of cluster-based materials

A. Fischer, H. Gleiter, and H. Hahn, Frühjahrstagung der Deutschen Physikalischen Gesellschaft, Fachverband Metall- und Materialphysik, March 25–30, 2012, *Berlin*.

Design and construction of an apparatus for the deposition of mass selected metal clusters

A. Fischer, H. Gleiter, and H. Hahn, Frühjahrstagung der Deutschen Physikalischen Gesellschaft, Fachverband Dünne Schichten, March 13–18, 2011, *Dresden*.

Optical Hyperfine Structure and Isotope Shift Measurements on Os^-

A. Fischer, C. Canali, U. Warring, and A. Kellerbauer, Frühjahrstagung der Deutschen Physikalischen Gesellschaft, Fachverband Atomphysik, March 02–06, 2009, *Hamburg*.